UNIVERSITY OF CALIFORNIA
SANTA CRUZ

RECONSTRUCTING SHAPES FROM SUPPORT AND BRIGHTNESS FUNCTIONS

A thesis submitted in partial satisfaction of the
requirements for the degree of

MASTER OF SCIENCE

in

COMPUTER ENGINEERING

by

Amyn Poonawala

March 2004

The Thesis of Amyn Poonawala
is approved:

Professor Peyman Milanfar, Chair

Professor Richard Gardner

Professor Roberto Manduchi

Professor Hai Tao

Robert C. Miller
Vice Chancellor for Research and
Dean of Graduate Studies

Contents

List of Figures

Abstract

Reconstructing Shapes from Support and Brightness Functions

by

Amyn Poonawala

In many areas of science and engineering, it is of interest to obtain the shape of an object or region from partial, weak, and indirect data. Such type of problems are referred to as geometric inverse problems. In this thesis, we analyze the inverse problems of reconstructing a planar shape using two different (but related) type of information, namely, support function data and brightness function data. The brightness function measurement along a viewing direction gives the volume of the orthogonal projection of the body along that direction. We discuss linear and non-linear estimation algorithms for reconstructing a planar convex shape using finite and noisy measurements of its support and brightness functions. The shape is parameterized using its Extended Gaussian Image (EGI). This parameterization allows us to carry out a systematic statistical analysis of the problem via a statistical tool called the Cramer-Rao lower bound (CRLB). Using CRLB, we develop uncertainty regions around the true shape using confidence region visualization techniques. Confidence regions conveniently display the effect of experimental parameters like eccentricity, scale, noise, viewing direction set, on the quality of estimated shapes. Finally, we perform a statistical performance evaluation of our proposed algorithms using confidence regions.

To my parents, Daulat and Alaudin Poonawala

Acknowledgements

I would like to express my deep and sincere gratitude to my advisor Dr. Peyman Milanfar for giving me the opportunity to work on this problem and providing invaluable guidance. His dynamism, vision, and motivation have deeply inspired me and his valuable suggestions helped me to seek the right direction in research.

I also wish to thank Dr. Richard Gardner for his active engagement, insightful discussions and inculcating me with good writing skills. I also thank my other committee members Dr. Roberto Manduchi and Dr. Hai Tao for their comments and suggestions.

Special thanks to my wonderful colleagues at the Multi-Dimensional Signal Processing (MDSP) group Morteza Shahram, Dirk Robinson, Sina Farsiu and my office-mates Li Rui and Dr. YuanWei Jin for several fruitful discussions. I also thank my friends at UCSC Srikumar, Sanjit, Ashwani, Chandu, Shomo, and everybody else; your presence made my graduate life a wonderful treasurable experience. Also my gratitude to the terrific JEA gang Salim (Nayu), Amin (Pyala), Salim (Fugga), Murad (Pandey), and Altaf (Kaalu).

Above all, the love, care, patience, and support of my Mom, Dad and my brother Azim. I could do this only because of the virtues, values, and confidence you instilled in me; this work is dedicated to you.

Santa Cruz, CA March 18, 2004 Amyn Poonawala

Chapter 1

Introduction

In this chapter we briefly introduce the problems of shape reconstruction from support and brightness functions. We discuss the applications where such type of data can be extracted from physical measurements and also discuss related problems which have been studied in the past by various researchers. Finally, we present the organization of this thesis.

1.1 Support Functions

A support line of an object is a line that just touches the boundary of the object. If the shape is convex then the shape lies completely to one of the half-planes defined by its support lines. Furthermore, a convex body is uniquely defined by its support lines at all orientations (see [39, p. 38]). The support function $h(\alpha)$ along a viewing direction α is the distance from the origin to a support line which is orthogonal to the given direction (see Fig. 2.1).

The problem under consideration is that of reconstructing a shape using noisy measurements of its support function values. An early contribution in this area is accredited to Prince and Willsky [36] and [37]. Their study was motivated by the problem of Computed Tomography (CT) where the nonzero extent of each transmission projection provides support measurements of the underlying mass distribution. Prince and Willsky used support functions as priors to improve the performance of CT particularly when only limited data are available.

Support functions find diverse applications in various fields of science and engineering and hence they have been studied by several researchers in the past. Lele, Kulkarni, and Willsky [27] used support function measurements in target reconstruction from range-resolved and doppler-resolved laser-radar data. The general approach in [37] and [27] is to fit a polygon or polyhedron to the data, in contrast to that of Fisher, Hall, Turlach, and Watson [6], who use spline interpolation and the so-called von Mises kernel to fit a smooth curve to the data in the 2-D case. This method was taken up in [16] and [33], the former dealing with convex bodies with corners and the latter giving an example to show that the algorithm in [6] may fail for a given data set. Further studies and applications including 3-D can be found in [14], [20], and [22].

The problem of shape reconstruction from support function data has also been extensively studied by the Robotics community in order to reconstruct unknown shapes using probing. A line probe consists of choosing a direction in the plane and moving a line perpendicular to this direction from infinity until it touches the object.

Thus each line probe provides a supporting line of the object. Li [29] gave an algorithm that reconstructs convex polygons with $3V + 1$ (where V is the number of vertices) line probes and proved that this is optimal. Lindenbaum and Bruckstein [31] gave an approximation algorithm for arbitrary planar convex shapes to a desired accuracy using line probes. Unfortunately, most of the work in this field assumes pure measurements (no noise) and therefore it is more focussed towards the issues of computational and algorithmic complexity rather than estimation and uncertainty analysis.

1.2 Brightness Functions

A related problem (with weaker data) is that of shape reconstruction from noisy measurements of the brightness function. The *brightness function* of an n-dimensional body gives the volumes of its $(n-1)$-dimensional orthogonal projections (i.e., shadows) on hyperplanes. The problem is important in geometric tomography, the area of mathematics concerning the retrieval of information about a geometric object from data about its sections or projections (see [7]). For a 3-D body, the brightness function measurement along a viewing direction gives the area of the orthographic silhouette of the body along that direction.

In an imaging scenario, a brightness function measurement of an object can be obtained by counting the total number of pixels covered by the object in its image. One could also image an object using a single pixel CCD camera, for example, a photodiode element, and the brightness function is then proportional to the intensity of this pixel. We stress at the outset the extremely weak nature of such data. Each measurement provides a single scalar that records only the content of the shadow and nothing at all about its position or shape neither can we detect holes in it. Hence we restrict our attention to convex bodies (i.e. convex sets with non-empty interiors). In fact the brightness function is weak to the extent that there can be infinitely many bodies having the same (exact) brightness function measurement from all viewing directions.

Brightness function data appear as one of the several related types of data in the general inverse problem of reconstructing shape from projections. This has been treated in the past by mathematicians and researchers from the signal processing and computer vision community, and we now provide some hints to the voluminous literature on this topic.

Firstly, the term “projection” is (unfortunately and unnecessarily) often used in a very different (but not unrelated) sense, for what is also called an *X-ray* of an object. There are many successful algorithms for reconstructing images from X-rays, typically utilizing the Fourier or the Radon transform. Applications include radio astronomy, electron microscopy, and medical imaging techniques like the CAT (Computerized Axial Tomography) scan and PET (Positron Emission Tomography) scan. This is a huge subject in its own right; see, for example, [17] or [21]. Note that an X-ray of an object in a given direction provides an enormous amount of information. In particular, the support of the X-ray (the points in its domain at which it takes non-zero values) is just the orthogonal projection or shadow of the object.

There is also a considerable body of work on reconstructing a shape from its orthogonal projections given as sets. Thus one has multiple *silhouette* images along known viewing directions. These can be used to construct a visual-hull of the object (see for example [35], [1], [26], and the references in [7, Note 3.7] to geometric probing in computer vision). Very recently, Boltino, et al in [2] have also dealt with a weaker problem of reconstructing shapes from silhouettes with unknown position of the viewpoints. Shape-from-Silhouettes (SFS) is a very popular method and finds several applications such as non-invasive 3D model acquisition, obstacle avoidance and human motion tracking and analysis.

Note that a silhouette provides much weaker information than an X-ray, and, in general, a brightness function measurement similarly provides much weaker information still than a silhouette, since it merely records the area of the silhouette.

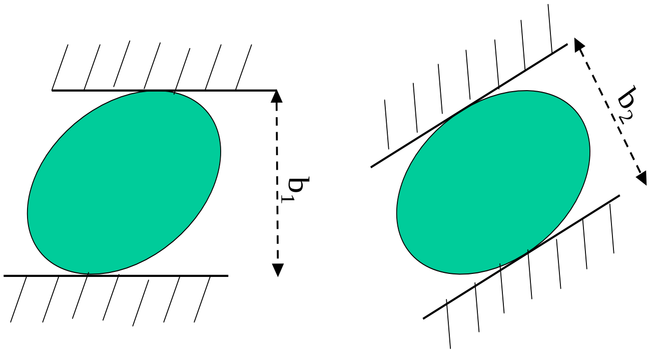

Figure 1.1: A tactile sensor grasping an object from 2 different orientations

In the 2-D case, the brightness function gives the lengths of the orthogonal projections of the shape on lines (see Fig. 2.2). Each measurement is then equal to the width of the shape orthogonal to the direction of the projection. The $\pm\pi/2$ phase-shifted version of brightness function in the planar case is referred to as the diameter function or width function in the robotics and computer vision community. Diameter measurements can also be obtained as the sum of support-line measurements along two antipodal directions. Shape from diameter has also been extensively studied by the robotics community where the diameter of an object can be measured using an instrumented parallel jaw-gripper as in Fig. 1.1). Rao and Goldberg [38] observed that diameter cannot be used to uniquely reconstruct shapes; instead they used them for recognizing a shape from a known (finite) set of shapes. Lindenbaum and Bruckstein [30] showed that shape can be uniquely reconstructed from binary perspective projections using $3V - 3$ measurements and proved this to be optimal. However, as with support functions, this work assumes pure measurements and pays more attention to algorithmic complexity.

1.3 Thesis Contribution and Organization

This thesis addresses the problem of reconstructing the shape of a planar convex object from finite, noisy and possibly sparse measurements of the support and brightness functions along a known set of viewing directions. Though this is not valid for higher dimensions, we shall collectively refer to support, diameter and brightness functions as support-type data. The shape is parameterized using its Extended Gaussian Image (EGI) because this parameterization facilitates a systematic statistical analysis of the problem. Using EGI, a polygon is encoded in terms of the lengths a_k

of its edges and their outer normal angles θ_k.

The thesis addresses two important aspects of the two inverse problems under consideration. First, we focus on non-linear and linear estimation algorithms for reconstructing shape from noisy support-type data. For support function measurements our approach is novel in that the approximating shape, a convex polygon, is parameterized using its Extended Gaussian Image (EGI). Second, we present a systematic statistical analysis of the problem via the Cramer-Rao lower bound and confidence region analysis. As a byproduct of the statistical analysis, we also introduce for the first time, a correct method for reconstructing planar shapes using corrupted EGI.

The reconstruction problem is solved in two steps; the first step consists of estimating the unknown EGI parameters from the noisy data and the second step translates the estimated EGI values to a more direct Cartesian representation (see Fig. 1.2). In addition to facilitating the statistical analysis, this approach has the advantage that the EGI of the object is estimated directly. This finds applications in machine vision problems like recognition, determining the attitude of an object, etc.

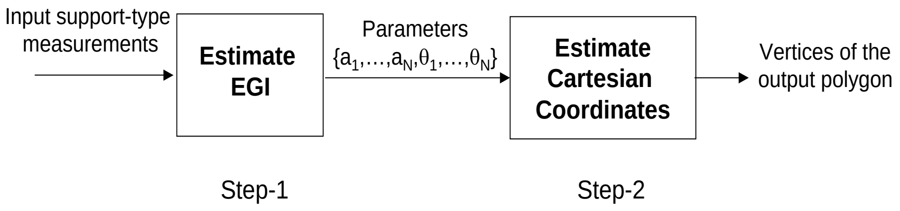
Input support-type measurements
Estimate EGI
Parameters
$\{a_1,\ldots,a_N,\theta_1,\ldots,\theta_N\}$
Estimate Cartesian Coordinates
Vertices of the output polygon
Step-1
Step-2

Figure 1.2: The two-step approach for estimating shape from support-type functions

In Chapter two, we explain the problems of shape from support and brightness functions in more detail followed by an introduction of the EGI parameterization.

The second step in Fig. 1.2, addressing the inverse problem of finding a shape from its EGI, is of considerable interest in its own right. Applications include astrophysics [25], computer vision [28], [32], the reconstruction of a cavity from ultrasound [41], and estimation of the directional distribution of a fiber process [24]. At first sight the problem seems a trivial one in the 2-D case, but the obvious method described in Section 2.3 was shown by our statistical study to be unsatisfactory. A completely new method we claim to be the correct one is introduced in Section 2.3.1. The same problem in three dimensions remains open. Finally in Section 2.4 we define the mathematical model for support-type measurements under the EGI parameterization.

Chapter three starts with a discussion of the previous algorithms for shape reconstruction from corrupted support function measurements. We propose novel linear and non-linear estimation algorithms for shape estimation using support-line measurements under the EGI parameterization. In Section 3.3 is a discussion of algorithms for reconstruction from noisy brightness function data. For exact measurements, these were introduced by Gardner and Milanfar [9], [10] and were proved in [10] to converge in any dimension when the convex body is origin symmetric, a requirement needed for uniqueness. By "converge," we mean that the outputs of the algorithms converge in the Hausdorff metric to the input convex body as the number of measurement directions increases through a sequence of directions whose union is dense in the unit sphere. In forthcoming joint work with Kiderlen [8], it will be shown that these algorithms, as well as those using the support function, still converge with noisy data. (Such convergence results seem to be rare. In particular, the algorithm in [6] is only proved to converge with probability approaching one as the number of measurement directions increases.) In this sense the algorithms we present are fully justified.

In Chapter five, we present sample output reconstructions obtained using the algorithms discussed in Chapter four for both support and brightness function measurements. We study the effect of experimental parameters like noise power, number of measurements, eccentricity and scale of the underlying polygon, on the quality of the estimated shape using Monte-Carlo simulations.

The statistical analysis itself is presented in Chapter five. Again, the approach for this type of reconstruction problem is new, involving the derivation of the constrained Cramér-Rao lower bound (CCRLB) on the estimated parameters. Using the CCRLB, local and global confidence regions can be calculated corresponding to any preassigned confidence level. These form uncertainty regions around points in the boundary of the underlying object, or around its whole boundary. Such confidence regions are tremendously powerful in displaying visually the dependence of measurement direction set, noise power, and the eccentricity, scale, and orientation of the underlying true shape on the quality of the estimated shape.

The confidence regions also assist us in doing a statistical performance analysis of the proposed algorithms which is presented in Chapter six. Performance analysis can be carried out using either local confidence regions as in Section 6.1 or using global confidence regions as in Section 6.2. We also present some more experimental results of the reconstructed polygons together with their local and global confidence regions in this section.

Finally, in Chapter seven, we introduce another exciting inverse problem called shape from *lightness functions* which forms an interesting direction of future research, and we present conclusive remarks for this thesis.

Chapter 2

Support-type functions and the EGI

In this chapter, we discuss the mathematical models for support and brightness function measurements. We introduce the EGI (Extended Gaussian Image) parameterization of a 2-D shape and also define support and brightness function data using the EGI parameterization.

2.1 Background

The support line $L_{\mathbf{S}}(\alpha)$ of the convex set S at angle α is a line orthogonal to the unit vector $\mathbf{v} = [\cos(\alpha), \sin(\alpha)]^T$ that just grazes the set S such that the shape lies completely in one of the half-planes defined by $L_{\mathbf{S}}(\alpha)$ (see Fig. 2.1). Its equation is given as,

$$L_{\mathbf{S}}(\alpha) = \{\mathbf{x} \in \Re^2 | \mathbf{x}^{\mathbf{T}}\mathbf{v} = h_{\mathbf{S}}(\alpha)\}, \tag{2.1}$$

where,

$$h_{\mathbf{S}}(\alpha) = \sup_{\mathbf{x}\in\mathbf{S}} \mathbf{x^T v}. \tag{2.2}$$

The magnitude of support function, i.e., $|h_{\mathbf{S}}(\alpha)|$ is the minimum distance from the origin to the support line $L_{\mathbf{S}}(\alpha)$.

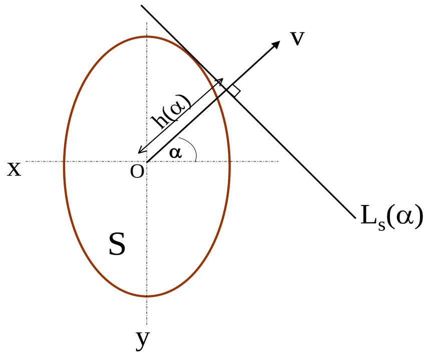

Figure 2.1: Support-line measurement of a planar body.

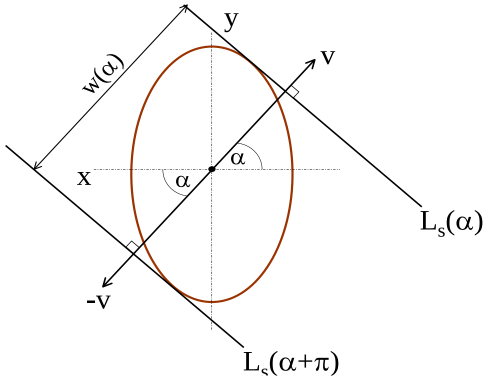

Figure 2.2: Diameter measurement of a planar body.

$h_{\mathbf{S}}(\alpha)$ is continuous and periodic with period 2π. A convex set can be completely determined by its support function measurements obtained from all viewing directions ([39], p. 38). However in practice, we only have a finite number of support function measurements $\mathbf{h} = [h(\alpha_1), h(\alpha_2), \ldots, h(\alpha_M)]^T$. Therefore there is a family of sets having the same support vector $\mathbf{h}$. The largest of these sets, a polygon $\mathbf{S_P}$, that is uniquely determined by $\mathbf{h}$ can be obtained by the intersection of the half-planes defined by support-lines as follows,

$$\mathbf{S_P} = \{\mathbf{x} \in \Re^2 | \mathbf{x}^T[\mathbf{v}_1, \mathbf{v}_2, \ldots, \mathbf{v}_M] \leq [h_1, h_2, \ldots, h_M]\}. \tag{2.3}$$

If $\mathbf{z_t} = (x_t, y_t)$ for $t = 1, \ldots, N$ are the vertices of the N-sided convex polygon $\mathbf{S_P}$, the support function

$$h_{\mathbf{S_P}}(\alpha) = \mathrm{max}_t(x_t \cos\alpha + y_t \sin\alpha). \tag{2.4}$$

For planar shapes, another closely related measurement is its width function. The width function is calculated as the sum of support-line measurement along two antipodal directions (see Fig. 2.2), i.e.,

$$w(\alpha) = h(\alpha) + h(\alpha + \pi). \tag{2.5}$$

Thus the width function is continuous and periodic with a period of π. The brightness function is simply a phase shifted version of the width function,

$$b(\alpha) = w(\alpha + \pi/2) = h(\alpha + \pi/2) + h(\alpha - \pi/2). \tag{2.6}$$

Therefore, in the planar case, the brightness function measures the length of the orthogonal projection (silhouette) of the shape. Each measurement $b(\alpha)$ provides a single scalar that records the length of the silhouette viewed from angle α and nothing at all about its position. Whereas a planar convex body is uniquely determined by all its silhouettes, there can be infinitely many number of bodies having the same (exact) brightness function measurements along all viewing directions. For example, all the three polygons on the left hand side in Fig. 2.3 have the same brightness function measurements and similarly the two bodies on the right hand side have equal (and even constant) brightness function values from all viewing directions. Thus, the brightness function does not uniquely determine a convex body even up to translation.

It is also true that for each convex body, there is an origin-symmetric body having the same brightness function values. An origin symmetric body is one equal

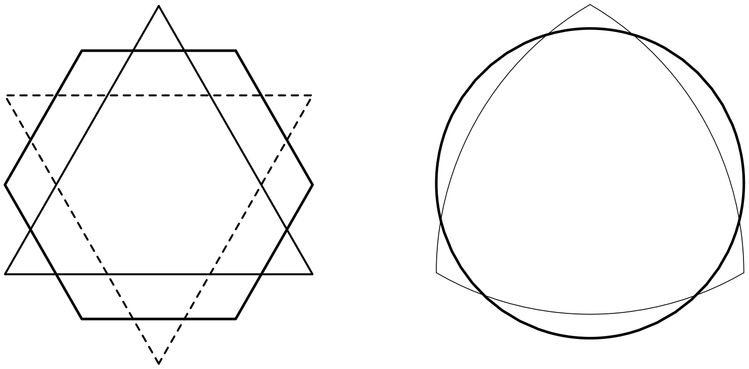

Figure 2.3: Non-uniqueness issue with brightness functions.

to its reflection in the origin. For detailed discussions, see [7, Chapter 3] and [10]. However, a remarkable result due to Alexandrov [7, Theorem 3.3.6] called Alexandrov's projection theorem, states that any two origin-symmetric convex bodies having the same brightness function must be equal. By seeking to reconstruct only origin-symmetric bodies, we therefore overcome the non-uniqueness problem for brightness functions. For example, in Fig. 2.3 the hexagon and the circle are origin symmetric bodies and hence our algorithm reproduces them uniquely as outputs.

2.2 Extended Gaussian Image

Underlying our whole approach is the idea of parameterizing a shape using its Extended Gaussian Image (EGI), also referred to as the Extended Circular Image in the 2-D case. EGI is obtained by mapping the surface normal vector information of an object onto the unit sphere (the unit circle in the 2-D case) called the Gaussian sphere. Each region of the unit sphere (unit circle in 2-D) is assigned a weight equal to the area (length in 2D) of the set of points on the surface of the shape at which the outer unit normal vector lies in the region. The EGI has the desirable property that it determines a convex object uniquely (up to translation). For more details, we refer the reader to [39] and [18].

When the shape is a suitably smooth convex body, the EGI can be represented by a function $f(u)$, where u is a unit vector and $f(u)$ is the reciprocal of the Gaussian curvature of the surface of the body at the point where the outer unit normal is u; see [10]. Thus in effect the EGI encodes the shape in terms of its curvature as a function of the outer unit normal to its boundary.

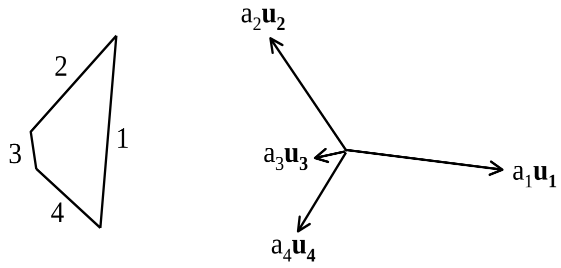

Figure 2.4: EGI vectors of a polygon.

When the shape is a convex polygon (or more generally, an n-dimensional convex polyhedron), the EGI is simple to describe. For an N-sided polygon whose kth edge has length a_k and outer unit normal vector u_k, the EGI is a measure on the unit circle consisting of a finite sum of point masses, each placed at the outer unit normal to an edge and having weight equal to the length of that edge. In other words, it becomes

$$f(u) = \sum_{k=1}^{N} a_k \delta(u - u_k), \tag{2.7}$$

where δ is the Dirac delta function. As Fig. 2.4 indicates, the EGI of an N-sided polygon can therefore be represented by the N vectors $a_k u_k$, each normal to an edge of the polygon and with magnitude equal to the length of that edge.

If $\mathbf{u_i} = [\cos(\theta_i), \sin(\theta_i)]^T$, the EGI of the polygon is equivalent to the set $\{a_1, \ldots, a_N, \theta_1, \ldots, \theta_N\}$, and this provides a convenient set of parameters we shall later use.

The important question naturally arises as to which sets $\{a_1, \ldots, a_N, \theta_1, \ldots, \theta_N\}$ of $2N$ real numbers correspond to the EGI of a convex polygon. The following necessary and sufficient conditions result from *Minkowski's existence theorem* (see [7, p. 356] or [39, p. 390]):

$$a_k \geq 0 \quad \text{for} \quad k = 1, \ldots, N \tag{2.8}$$

and the EGI vectors sum to zero, that is,

$$\sum_{k=1}^{N} a_k \mathbf{u}_k = \left[\sum_{k=1}^{N} a_k \cos\theta_k, \sum_{k=1}^{N} a_k \sin\theta_k \right]^T = [0, 0]^T. \tag{2.9}$$

2.3 Shape from EGI

As discussed in Section 1.3, step two of our reconstruction algorithm consists of obtaining the cartesian coordinates of the polygon from its EGI (see Fig. 1.2). The simplest way to achieve this is to arrange the vectors in counterclockwise order, rotate each vector counterclockwise by $\pi/2$, and place them so that the tail of each vector lies at the head of the preceding vector (see Fig. 2.5 and [32]). Then, if the given EGI is $\{a_1, \ldots, a_N, \theta_1, \ldots, \theta_N\}$, the vertices of the reconstructed polygon are

$$z_t = \sum_{k=1}^{t} a_k e^{i(\theta_k + \pi/2)}, \tag{2.10}$$

where $z_t = x_t + iy_t$ is the complex number representing the vertex $z_t = (x_t, y_t)$, $t = 1, \ldots, N$.

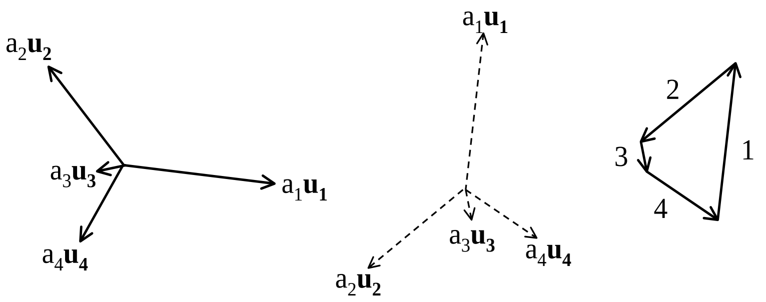

Given EGI vectors

EGI rotated by π/2

Reconstructed shape

Figure 2.5: Obtaining the Cartesian coordinate representation from the EGI.

While the above method using (2.10) is valid for pure EGI values, in the case of noisy EGI values, it is inadequate. The reason is that this method does not determine the vertices independently; rather, the position of each estimated vertex depends on that of the preceding estimated vertices. This causes the error in vertex position to accumulate as the vertex index t increases from $t = 1$ to N. A better method for reconstructing shape using noisy EGI is called for. In this section, we propose a novel statistically motivated method for estimating shape using noisy EGI values. We also prove for a simple case that the proposed method outperforms (2.10).

2.3.1 Proposed Method

Our basic aim is estimate $\mathbf{z} = [z_1, \ldots, z_N]^T$ so that the error is evenly distributed among the vertices. From (2.10) we have

$$z_t - z_{t-1} = a_t e^{i(\theta_t + \pi/2)}, \tag{2.11}$$

for $t = 1, \ldots, N$, and hence the equation

$$\mathbf{Qz} = \mathbf{r}, \tag{2.12}$$

where

$$\mathbf{Q} = \begin{bmatrix} -1 & 1 & 0 & \cdots & 0 & 0 \\ 0 & -1 & 1 & \cdots & 0 & 0 \\ \vdots & \vdots & \vdots & & \vdots & \vdots \\ 0 & 0 & 0 & \cdots & -1 & 1 \\ 1 & 0 & 0 & \cdots & 0 & -1 \end{bmatrix} \tag{2.13}$$

and

$$\mathbf{r} = \left[a_1 e^{i(\theta_1 + \pi/2)}, \ldots, a_N e^{i(\theta_N + \pi/2)}\right]^T.$$

However, $\operatorname{rank} \mathbf{Q} = N - 1$ and so the solution for $\mathbf{z}$ in (2.12) is not unique. We overcome this by fixing the barycenter of the vertices of the polygon (that is, their average) at the point with complex number form c by adding the constraint

$$\sum_{t=1}^{N} z_t = c. \tag{2.14}$$

When c is the origin, this can be written in the form $\mathbf{e}^T\mathbf{z} = 0$, where $\mathbf{e} = [1, 1, \ldots, 1]^T$. We can now solve the well-defined least-squares problem,

$$\min_{\mathbf{z}} \|\mathbf{Qz} - \mathbf{r}\|^2 + (\mathbf{e}^T\mathbf{z})^2. \tag{2.15}$$

The solution is a point where the derivative of the cost function becomes zero. Therefore,

$$\frac{d}{d\mathbf{z}}\left(||\mathbf{Qz} - \mathbf{r}||^2 + (\mathbf{e^T z})^2\right) = \frac{d}{d\mathbf{z}}\left(\mathbf{z^T Q^T Q z} - \mathbf{2 z^T Q^T r} + \mathbf{r^T r} + \mathbf{z e e^T z}\right) = 0. \tag{2.16}$$

This yields the unique solution,

$$\mathbf{z} = (\mathbf{Q}^T\mathbf{Q} + \mathbf{e}\mathbf{e}^T)^{-1}\mathbf{Q}^T\mathbf{r} = \mathbf{D}\mathbf{r}, \tag{2.17}$$

where we note that the matrix being inverted is now full rank. Let d_{ij} for $i, j = 1, \ldots, N$ represent the elements of the matrix $\mathbf{D}$. Therefore,

$$z_t = \sum_{k=1}^{N} d_{tk} a_k e^{i(\theta_k + \pi/2)}, \tag{2.18}$$

for $t = 1, \ldots, N$. Comparing (2.18) with (2.10), we see that z_t now depends on all the EGI vectors.

2.3.2 A basic statistical comparison of the two methods

From Fig. 1.2 we note that the EGI is estimated from the noisy input support-type data and therefore it too will be corrupted. Let $\hat{\mathbf{a}} = [\hat{a}_1, \ldots, \hat{a}_N]^T$ and $\hat{\boldsymbol{\Theta}} = [\hat{\theta}_1, \ldots, \hat{\theta}_N]^T$ correspond to the estimated EGI components. For the sake of simplicity in our analysis, let us assume that the angles are estimated accurately, i.e. $\hat{\boldsymbol{\Theta}} = \boldsymbol{\Theta}$, thereby leaving $\hat{\mathbf{a}}$ as the only corrupted data. We further assume that the elements of $\hat{\mathbf{a}}$ have identical variances and are uncorrelated to each other. Then the covariance of $\hat{\mathbf{a}}$ is

$$\mathrm{cov}(\hat{\mathbf{a}}) = \begin{bmatrix} \sigma^2 & 0 & 0 & \cdots & 0 \\ 0 & \sigma^2 & 0 & \cdots & 0 \\ \vdots & \vdots & \vdots & & \vdots \\ 0 & 0 & 0 & \cdots & \sigma^2 \end{bmatrix} = \sigma^2 \mathbf{I}. \tag{2.19}$$

From (2.10), the estimated polygon $\hat{\mathbf{z}}$ is given as,

$$\hat{\mathbf{z}} = \mathbf{P}\hat{\mathbf{r}} \tag{2.20}$$

where,

$$\mathbf{P} = \begin{bmatrix} 1 & 0 & 0 & \cdots & 0 & 0 \\ 1 & 1 & 0 & \cdots & 0 & 0 \\ \vdots & & & & & \\ 1 & 1 & 1 & \cdots & 1 & 1 \end{bmatrix} \tag{2.21}$$

and,

$$\hat{\mathbf{r}} = \left[\hat{a}_1 e^{i(\theta_1+\pi/2)}, \hat{a}_2 e^{i(\theta_2+\pi/2)}, \ldots, \hat{a}_N e^{i(\theta_N+\pi/2)}\right]^T. \tag{2.22}$$

Now, $\text{cov}(\hat{\mathbf{z}}) = \mathbf{P}\text{cov}(\hat{\mathbf{r}})\mathbf{P^T}$. Hence, our next task is to calculate the covariance of $\hat{\mathbf{r}}$. We note that $\hat{\mathbf{r}}$ can be written as,

$$\hat{\mathbf{r}} = \begin{bmatrix} e^{i(\theta_1+\pi/2)} & 0 & \cdots & 0 & 0 \\ 0 & e^{i(\theta_2+\pi/2)} & \cdots & 0 & 0 \\ \vdots & & & & \\ 0 & 0 & \cdots & e^{i(\theta_{N-1}+\pi/2)} & 0 \\ 0 & 0 & \cdots & 0 & e^{i(\theta_N+\pi/2)} \end{bmatrix} \begin{bmatrix} \hat{a}_1 \\ \hat{a}_2 \\ \vdots \\ \hat{a}_{N-1} \\ \hat{a}_N \end{bmatrix} = \mathbf{R_\Theta}\hat{\mathbf{a}} \tag{2.23}$$

Therefore,

$$\begin{aligned} \text{cov}(\hat{\mathbf{r}}) &= \mathbf{R_\Theta}\text{cov}(\hat{\mathbf{a}})\mathbf{R_\Theta}^{\mathbf{H}} \\ &= \mathbf{R_\Theta}\mathbf{R_\Theta}^{\mathbf{H}}\text{cov}(\hat{\mathbf{a}}) \qquad (\text{cov}(\hat{\mathbf{a}}) \text{ and } \mathbf{R_\Theta} \text{ are diagonal matrices}) \end{aligned}$$

$$
\begin{aligned}
&= (\mathbf{I})\ \mathrm{cov}(\hat{\mathbf{a}}) && (\mathbf{R}_{\boldsymbol{\Theta}} \text{ is a unitary matrix}) \\
&= \sigma^2 \mathbf{I} && (\text{from } 2.19) \qquad (2.24)
\end{aligned}
$$

Therefore,

$$\mathrm{cov}(\hat{\mathbf{z}}) = \sigma^2(\mathbf{P}\mathbf{P}^{\mathbf{T}}) \qquad (2.25)$$

The variances of the individual estimated vertices are given by the diagonal elements of the above matrix. By observing the structure of the matrix $\mathbf{P}$, it is not difficult to see that these diagonal elements are increasing linearly as a function of the index t. More explicitly,

$$\mathbf{P}\mathbf{P}^T = \begin{bmatrix} 1 & 1 & 1 & \cdots & 1 \\ 1 & 2 & 2 & \cdots & 2 \\ 1 & 2 & 3 & \cdots & 3 \\ \vdots & \vdots & \vdots & & \vdots \\ 1 & 2 & 3 & \cdots & N \end{bmatrix},$$

which leads to,

$$\mathrm{var}(\hat{z}_t) = \sum_{i=1}^{t} \sigma^2 \qquad (2.26)$$

for $t = 1, \ldots, N$

Equation (2.26) clearly demonstrates that the variance of the estimated vertex increases as the index increases (accumulation effect). This is highly undesirable and therefore (2.10) is not an optimum method for estimating cartesian coordinates from EGI.

Next we demonstrate that the proposed method (2.18) overcomes this issue. From (2.17), $\hat{\mathbf{z}} = \mathbf{D}.\hat{\mathbf{r}}$, therefore, $\text{cov}(\hat{\mathbf{z}}) = \mathbf{D}\text{cov}(\hat{\mathbf{r}})\mathbf{D}^{\mathbf{T}}$. Employing the same assumptions and arguments as earlier, we note that,

$$\text{cov}(\hat{\mathbf{z}}) = \sigma^2(\mathbf{D}\mathbf{D}^{\mathbf{T}}) = \sigma^2(\mathbf{Q}^T\mathbf{Q} + \mathbf{e}\mathbf{e}^T)^{-1}\mathbf{Q}^T\mathbf{Q}(\mathbf{Q}^T\mathbf{Q} + \mathbf{e}\mathbf{e}^T)^{-1}. \tag{2.27}$$

By (2.13), $\mathbf{Q}$ is a square circulant matrix, and since $\mathbf{e} = [1, 1, \ldots, 1]^T$, the matrix $\mathbf{e}\mathbf{e}^T$ has every entry equal to 1 and is therefore also a square circulant matrix. Using the well-known facts that the sum, product, transpose, and inverse of square circulant matrices are again square circulant matrices [4], we see from (2.27) that $\text{cov}(\hat{\mathbf{z}})$ is also a square circulant matrix. Therefore its diagonal elements are equal; in other words, the variances $\text{var}(\hat{z}_t)$, $t = 1, \ldots, N$ are all equal and hence the error is distributed more evenly amongst all the vertices. Moreover, the variances are independent of the index number of the vertices unlike (2.26).

Under our simplifying assumption, this demonstrates that the proposed method (2.18) is a statistically improved way of estimating the cartesian coordinates of a polygon from the corrupted EGI values. However, an extension of this problem to the 3-D case is more difficult. Little in [32] proposed a *non-linear* algorithm for reconstructing a 3-D shape from pure EGI values. The problem of 3-D shape reconstruction from noisy EGI has essentially not been treated by researchers in the past (so far as we are aware), thereby forming a challenging direction of future work.

2.4 Relation between support-type functions and the EGI

Here we define the mathematical model which will enable us to directly calculate the support and brightness function values of a shape from the EGI.

2.4.1 Support Functions

The support function of a polygon along a given viewing direction is defined using equation (2.4) which makes use of the *max* function. This is a combinatorial relation and cannot be used in this form for the inverse problem of estimating the shape. Let $[\theta_1, \ldots, \theta_N]^T$ be a vector consisting of the normals to each side of the polygon and $\mathbf{z_t} = [x_t, y_t]^T$ be the vertex formed by the intersection of the edges whose normals are along θ_t and θ_{t+1} respectively. From Fig 2.6 we observe that every viewing direction α can be thought of lying in a wedge defined by the two adjacent angles θ_t and θ_{t+1}. The support function measurement of the underlying polygon along α is solely dictated only one vertex $\mathbf{z_t}$ which falls inside the above wedge.

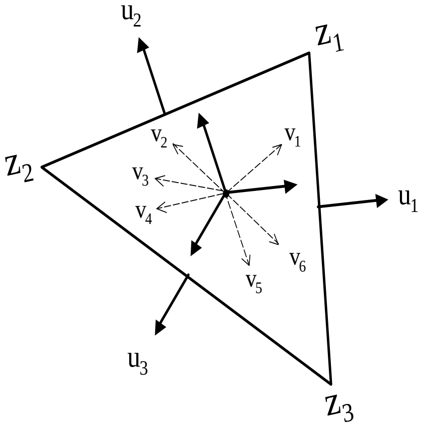

Figure 2.6: Viewing directions distributed amongst the wedges.

Thus, if $\theta_t \leq \alpha < \theta_{t+1}$, (2.4) can be simplified as,

$$h_S(\alpha) = x_t \cos(\alpha) + y_t \sin(\alpha). \tag{2.28}$$

Note that if we first assign the correspondence between the viewing angles and the wedges formed by the normals, we can get rid of the *max* function in (2.4). Using (2.18), we can write the vertex coordinates $\mathbf{z_t} = [x_t, y_t]^T$ of a polygon in terms of its EGI as follows,

$$\mathbf{z_t} = \left[\sum_{k=1}^{N} d_{tk} a_k \cos(\theta_k + \pi/2), \sum_{k=1}^{N} d_{tk} a_k \sin(\theta_k + \pi/2)\right]^T. \tag{2.29}$$

From (2.29) and (2.28) we obtain,

$$\begin{aligned} h_S(\alpha) &= \sum_{k=1}^{N} d_{tk} a_k \cos(\theta_k + \pi/2) \cos(\alpha) + \sum_{k=1}^{N} d_{tk} a_k \sin(\theta_k + \pi/2) \sin(\alpha), \\ &= \sum_{k=1}^{N} d_{tk} a_k \sin(\alpha - \theta_k). \end{aligned} \tag{2.30}$$

Note that the above expression is only valid for a polygon having the barycenter of its vertices at the origin. Thus, the support values of a polygon can be calculated from its EGI using (2.30).

2.4.2 Brightness Functions

We now proceed to defining the brightness function values of a shape using EGI. The brightness function $b(v)$ of a continuous body for a given viewing direction v (a unit vector) is given by [7],

$$b(v) = \frac{1}{2} \int_S |u^T v| f(u) du. \tag{2.31}$$

Integration is over the unit sphere (in two dimensions, the unit circle S). Since $|u^T v|$ is a cosine term, it is true that $|u^T v| f(u) du$ represents the area of the projection in the direction v of an surface element du normal to u (refer Fig. 2.7). Thus, the brightness function measurement along a given direction is the volume of the orthogonal projection of the body along that direction. It is important to note that the brightness functions data are scalar values (volume of projections), therefore they only provide a one-dimensional information about an n-dimensional body. As a result the brightness function data becomes progressively weaker as we move on to the higher dimensions.

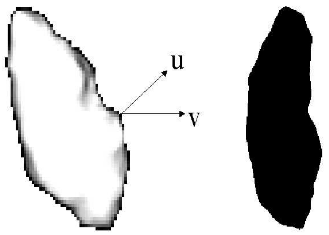

Figure 2.7: A 3-D object and its shadow in the direction v.

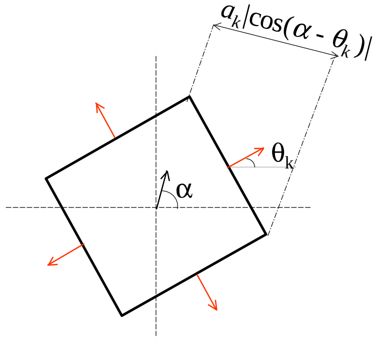

Figure 2.8: Projection of an edge.

For an N-sided convex polygon, $a_k|u_k^T v|$ is just the length of the projection of the kth edge in the direction v (see Fig. 2.8). The brightness function of this polygon is

$$b(v) = \frac{1}{2} \sum_{k=1}^{N} a_k |u_k^T v|. \tag{2.32}$$

(This formula can also be obtained by substituting (2.7) into (2.31), assuming this is valid.) If $v = [\cos\alpha, \sin\alpha]^T$ and $u_k = [\cos\theta_k, \sin\theta_k]^T$, we can rewrite (2.32) in the form

$$b(\alpha) = \frac{1}{2}\sum_{k=1}^{N} a_k|\cos(\alpha - \theta_k)|. \tag{2.33}$$

Thus, the brightness function values of a polygon can be calculated from its EGI using (2.33). We note here that $b(\alpha)$ can also be thought of as the circular convolution of the vector $\mathbf{a}$ with the function $|\cos(x)|$.

Chapter 3

Algorithms for shape from support-type functions

In this chapter, we propose linear and non-linear algorithms for estimating the EGI of a polygon from finite and noisy support-type measurements. We follow the two step approach for shape reconstruction outlined in Fig. 1.2.

3.1 Support functions

We consider an unknown planar convex body K with a finite number of noisy support function measurements modelled by, $y(\alpha_m) = h(\alpha_m)+n(\alpha_m)$ in fixed measurement directions $\mathbf{v}_m = [\cos\alpha_m, \sin\alpha_m]^T$, $m = 1, \ldots, M$. The noise $n(\alpha_m)$ is assumed to be white Gaussian noise with variance σ^2. Collecting the above measurements into a vector form,

$$\mathbf{y} = \mathbf{h} + \mathbf{n}, \tag{3.1}$$

where $\mathbf{y} = [y(\alpha_1), \ldots, y(\alpha_M)]^T$ is the observation vector, $\mathbf{h} = [h(\alpha_1), \ldots, h(\alpha_M)]^T$ is the vector of true support values and $\mathbf{n} = [n(\alpha_1), \ldots, n(\alpha_M)]^T$ is the noise vector. We now discuss some past algorithms for shape reconstruction from corrupted support function data.

3.1.1 Past Algorithms

Prince and Willsky [37] observed that because of the presence of noise, the measured support vector $\mathbf{y} = [y(\alpha_1), \ldots, y(\alpha_M)]^T$ may not correspond to *any* closed convex set $\mathbf{S}$. They derived the necessary and sufficient conditions, a set of inequality constraints, to check the consistency of the measured support vector $\mathbf{y}$ when the measurement angles are equally spaced. Lele, et al [27] extended their work by deriving the constraint set for the more practical case of any general measurement set.

Using (3.1), the estimated vector $\hat{\mathbf{h}}$ can be obtained by employing the constrained linear least squares optimization as (see [27]),

$$\hat{\mathbf{h}} = \arg\min_{\mathbf{h}} ||\mathbf{y} - \mathbf{h}||^2, \tag{3.2}$$

subject to the constraint,

$$\mathbf{C}(\boldsymbol{\Omega})\mathbf{h} \geq 0 \tag{3.3}$$

where $\boldsymbol{\Omega} = [\alpha_1, \ldots, \alpha_M]^T$ and,

$$\mathbf{C}(\boldsymbol{\Omega}) = \begin{bmatrix} -\sin(\alpha_2 - \alpha_M) & \sin(\alpha_1 - \alpha_M) & 0 & \ldots & \sin(\alpha_2 - \alpha_1) \\ \sin(\alpha_3 - \alpha_2) & -\sin(\alpha_3 - \alpha_1) & \sin(\alpha_2 - \alpha_1) & \ldots & 0 \\ 0 & \sin(\alpha_4 - \alpha_3) & -\sin(\alpha_4 - \alpha_2) & \ldots & 0 \\ \vdots & \vdots & \vdots & \vdots & \vdots \\ \sin(\alpha_M - \alpha_{M-1}) & 0 & 0 & \sin(\alpha_1 - \alpha_M) & -\sin(\alpha_1 - \alpha_{M-1}) \end{bmatrix}. \tag{3.4}$$

The constraint (3.3) is a necessary and sufficient condition, essentially due to Rademacher (see [39, p. 47], which includes an extension to higher dimensions), for $\mathbf{h}$ to be consistent with a support function of a closed convex set. From $\hat{\mathbf{h}}$, the output polygon can be reconstructed using the intersection method described in (2.3). Note that this method gives an M-sided output polygon irrespective of the number of sides of the underlying polygon.

The second method proposed by Lele, Kulkarni and Willsky in [27] makes use of prior information about the angles of sides of the object. The aim is to reconstruct an N-sided polygon with pre-specified normal directions to its sides using M corrupted support function measurements. Let $\theta_1, \ldots, \theta_N$ be the known angles of the sides of the underlying polygon. The shape is parameterized using its support function values at $\boldsymbol{\Theta}$ where $\boldsymbol{\Theta} = [\theta_1, \ldots, \theta_N]^T$. Hence, if a given measurement angle α_m lies anywhere in the wedge formed by two adjacent normals θ_{L_m} and θ_{R_m}, i.e. $\theta_{R_m} \leq \alpha_m \leq \theta_{L_m}$, then,

$$h(\alpha_m) = \frac{\sin(\theta_{R_m} - \alpha_m)}{\sin(\theta_{R_m} - \theta_{L_m})} h_{L_m} + \frac{\sin(\alpha_m - \theta_{L_m})}{\sin(\theta_{R_m} - \theta_{L_m})} h_{R_m}. \tag{3.5}$$

The support function measurement model in this case is,

$$\mathbf{y} = \mathbf{A}(\boldsymbol{\Theta})\mathbf{h} + \mathbf{n}, \tag{3.6}$$

where, $\mathbf{y}$ and $\mathbf{n}$ hold the same meaning as in (3.1) but $\mathbf{h} = [h(\theta_1), h(\theta_2), \ldots, h(\theta_N)]^T$. The matrix $\mathbf{A}(\boldsymbol{\Theta}) \in \Re^{M \times N}$ is defined using (3.5) which computes the support values along any direction α using the support values along two adjacent normals. Thus the mth row of $\mathbf{A}(\boldsymbol{\Theta})$ has two adjacent non-zero entries corresponding to angles θ_{L_m} and θ_{R_m} such that α_m lies in the interval $[\theta_{L_m}, \theta_{R_m}]$. Using (3.6), the estimated vector $\hat{\mathbf{h}}$

can be obtained by employing least squares optimization (see [27]),

$$\hat{\mathbf{h}} = \arg\min_{\mathbf{h}} ||\mathbf{y} - \mathbf{A}(\boldsymbol{\Theta})\mathbf{h}||^2, \tag{3.7}$$

subject to the constraint $\mathbf{C}(\boldsymbol{\Theta}) \geq 0$. The matrix $\mathbf{A}(\boldsymbol{\Theta})$ in (3.7) is completely determined and hence the optimization problem is linear in the unknown parameter $\mathbf{h}$.

3.1.2 Proposed Algorithms using EGI Parameterization

We use the two-step approach outlined in Fig. 1.2 to estimate shape from noisy support functions. In this section we discuss algorithms for estimating the EGI of a convex polygon using finite, noisy support line measurements. Once this is done, we can use (2.18) to obtain the cartesian coordinates of the polygon.

Here we deal with two cases; in the first case, the normal to the edges are either known or fixed a priori and therefore we estimate only the length of edges, whereas, in the second case the entire EGI vector (both length and normals) are estimated. The estimation algorithms are linear and non-linear for the aforementioned cases respectively.

Linear Algorithms

If we assume that the underlying shape K is an N-sided polygon whose vertices have barycenter at $\mathbf{0}$ and which has prescribed outer normal angles θ_k, $k = 1, \ldots, N$, then we proceed as follows. For each measurement angle α_m, we assign t_m

such that $\theta_{t_m} \leq \alpha_m < \theta_{t_{m+1}}$ and then use (2.30) and (3.1) to obtain

$$y(\alpha_m) = \sum_{k=1}^{N} d_{t_m k} a_k \sin(\alpha_m - \theta_k) + n(\alpha_m), \tag{3.8}$$

where the unknowns are the edge lengths a_k, $k = 1, \ldots, N$. In vector form this becomes the measurement model

$$\mathbf{y} = \mathbf{S}(\boldsymbol{\Theta})\mathbf{a} + \mathbf{n}, \tag{3.9}$$

where $\mathbf{y}$, $\boldsymbol{\Theta}$, and $\mathbf{n}$ have the same meaning as in (3.6), $\mathbf{a} = [a_1, \ldots, a_N]^T$, and the matrix $\mathbf{S}(\boldsymbol{\Theta}) \in \Re^{M \times N}$ has entries $\mathbf{S}(\boldsymbol{\Theta})_{m,k} = d_{t_m k} \sin(\alpha_m - \theta_k)$. We can then solve the least squares problem

$$\hat{\mathbf{a}} = \arg\min_{\mathbf{a}} ||\mathbf{y} - \mathbf{S}(\boldsymbol{\Theta})\mathbf{a}||^2, \tag{3.10}$$

subject to the Minkowski's condition give by (2.8) and (2.9) which ensure that the estimated EGI vector corresponds to a closed convex polygon. Since $\boldsymbol{\Theta}$ is known, $\mathbf{S}(\boldsymbol{\Theta})$ is completely determined and the constraints are linear in the unknown parameter $\mathbf{a}$; hence (3.10) is a constrained linear least squares optimization problem.

The linear algorithm based on (3.10) is equivalent to that of Lele, Kulkarni, and Willsky [27] described in (3.7); that is, for a given input vector $\mathbf{y}$ and prescribed outer normal angle vector $\boldsymbol{\Theta}$, the outputs of the two algorithms are the same (provided both algorithms construct polygons whose vertices have barycenter at $\mathbf{0}$). If we take $N = M$ and replace $\boldsymbol{\Theta}$ by $\boldsymbol{\Omega}$, the algorithm based on (3.10) is equivalent to that of Prince and Willsky [37] described in (3.2).

Non-linear algorithm

In this case, both normals and length of edges of the underlying polygon are unknown. However, we assume that the underlying polygon has its barycenter at the origin and that the correspondence between the viewing angles and the wedges (as explained in Fig. 2.6 and Section 2.4.1) is known a priori. Thus, for every measurement α_m, we know t_m such that $\theta_{t_m} \leq \alpha_m \leq \theta_{t_m+1}$. Under these assumptions, we can write the measurement model using (3.8) as,

$$\mathbf{y} = \mathbf{S}(\boldsymbol{\Theta})\mathbf{a} + \mathbf{n}. \tag{3.11}$$

However, in this case the unknowns are $a_1, \ldots, a_N$ and $\theta_1, \ldots, \theta_N$. Note that our prior assumption is weaker compared to Lele, et al in (3.6); they assumed that the normal directions of the edges are pre-specified, whereas in our case the normals are still unknown. Also, unlike (3.2), the number of sides of the reconstructed polygon are independent of the number of measured support values.

Employing the least-squares error criterion, the unknowns in (3.11) can be estimated as,

$$(\hat{\mathbf{a}}, \hat{\boldsymbol{\Theta}}) = \arg \min_{(\mathbf{a}, \boldsymbol{\Theta})} ||\mathbf{y} - \mathbf{S}(\boldsymbol{\Theta})\mathbf{a}||^{\mathbf{2}} \tag{3.12}$$

subject to the Minkowski constraints (2.8) and (2.9). Note that the optimization problem is non-linear in the unknown parameters. Moreover, this algorithm is actually the Maximum Likelihood Estimator (MLE) of the unknown parameters $\mathbf{a}$ and $\boldsymbol{\Theta}$ owing to the Gaussian noise assumption (see [23, pp. 223–6 and 254–5] for further details).

3.2 Algorithms for Shape from Brightness Functions

We now discuss algorithms for shape reconstruction using corrupted brightness function measurements. The problem is solved using the same two-step approach illustrated in Fig. 1.2. In this section we discuss linear and non-linear algorithms to estimate the EGI of a polygon from corrupted brightness function data.

We assume that the brightness function measurements are obtained from an N-sided polygon using the model $\tilde{b}(\alpha_m) = b(\alpha_m) + n(\alpha_m)$, $m = 1, \ldots, M$, where the first term is given by (2.33) and the second term is the noise. As before, the noise throughout the discussion is Gaussian white noise with variance σ^2. While the scope of this section is restricted to the planar case, the algorithms discussed in this section can be readily extended to higher dimensions (for more details see [10]).

In vector form the measurements are

$$\tilde{\mathbf{b}} = \mathbf{C}(\boldsymbol{\Theta})\mathbf{a} + \mathbf{n}, \tag{3.13}$$

where $\tilde{\mathbf{b}} = [\tilde{b}(\alpha_1), \ldots, \tilde{b}(\alpha_M)]^T$, $\mathbf{n} = [n(\alpha_1), \ldots, n(\alpha_M)]^T$, $\mathbf{a} = [a_1, \ldots, a_N]^T$, $\boldsymbol{\Theta} = [\theta_1, \ldots, \theta_N]^T$, and $\mathbf{C}(\boldsymbol{\Theta})_{mk} = |\cos(\alpha_m - \theta_k)|/2$. Employing the least-squares error criterion, the unknowns in (3.13) can be estimated as

$$(\hat{\mathbf{a}}, \hat{\boldsymbol{\Theta}}) = \arg \min_{(\mathbf{a}, \boldsymbol{\Theta})} \|\tilde{\mathbf{b}} - \mathbf{C}(\boldsymbol{\Theta})\mathbf{a}\|^2. \tag{3.14}$$

However, note that $\mathbf{a}$ and $\boldsymbol{\Theta}$ should define a convex polygon, therefore the optimization problem (3.14) is subject to the constraints (2.8) and (2.9).

In general, the solution to (3.14) is not unique, even when there is no noise in the measurements. This is to be expected in view of the, finite, weak nature of data. But in order to ensure a reasonable reconstruction, we also need to overcome the more serious non-uniqueness issue associated with brightness functions illustrated by Fig. 2.3. As per our discussion in Section 2.1, this can be achieved if we seek to reconstruct origin-symmetric convex bodies. The origin symmetry of our approximating polygon is ensured by imposing the following linear constraints on its EGI (note that N must be even in this case):

$$a_k = a_{N/2+k} \text{ for } k = 1, \ldots, N/2; \tag{3.15}$$

$$\theta_k = \theta_{N/2+k} + \pi \text{ for } k = 1, \ldots, N/2. \tag{3.16}$$

These two constraints imply (2.9) and hence make it redundant. To summarize, we solve (3.14), subject to (2.8), (3.15), and (3.16). This algorithm is the Maximum Likelihood Estimator (MLE) of the unknown parameters $\mathbf{a}$ and $\boldsymbol{\Theta}$ again owing to the Gaussian noise assumption. Since (3.14) is non-linear in the unknown parameters, constrained non-linear optimization is required, and this is computationally very expensive. Without adaptation, this algorithm is therefore of little practical use.

One possible adaptation is prompted by the observation that the least squares problem (3.14) is of a special type known as separable. It could then be feasible to use the variable projection method of Golub and Pereyra [12] where each of the unknowns $\mathbf{a}$ and $\boldsymbol{\Theta}$ is treated separately in each iteration. However, a different modification, using a theoretical result of Campi, Colesanti, and Gronchi [3], effectively allows (3.14) to be made linear. This result states that if K is a convex body and V is a finite set of unit vectors, then among all the convex bodies having the same brightness function as K in the directions in V, there is a unique convex body with maximal volume. Moreover, this body is an origin-symmetric convex polyhedron with each facet orthogonal to one of a certain set W of directions that can be calculated from V (see [10]). In the 2-D case, where V is the set α_m, $m = 1, \ldots, M$, the set W is simply $\alpha_m \pm \pi/2$, $m = 1, \ldots, M$. Therefore we can set $N = 2M$ and $\theta_k = \alpha_k + \pi/2$, $k = 1, \ldots, N/2$, the remaining unit outer normal vectors to the edges being defined by (3.16). This reduces (3.14) to a linear optimization problem where the only unknown parameters are $a_1, \ldots, a_N$, namely:

$$\hat{\mathbf{a}} = \arg\min_{\mathbf{a}} \|\tilde{\mathbf{b}} - \mathbf{C}(\boldsymbol{\Theta})\mathbf{a}\|^2, \tag{3.17}$$

subject to (2.9) and

$$a_k = a_{(N/2)+k} \text{ for } k = 1, \ldots, N/2. \tag{3.18}$$

Now (3.17) can be solved using constrained linear least squares optimization. From Fig. 2.5, we observe that an origin symmetric body can be completely defined using only half of its EGI vectors. Therefore, the optimization problem in (3.17) can be further simplified as,

$$\hat{\mathbf{a}} = \arg\min_{\mathbf{a}} \|\tilde{\mathbf{b}} - 2\mathbf{C}(\boldsymbol{\Theta})\mathbf{a}\|^2, \tag{3.19}$$

subject to (2.9) where, $N = M$, $\mathbf{a} = [a_1, \ldots, a_N]^T$, $\theta_k = \alpha_k + \pi/2$, $k = 1, \ldots, N$. Thus we estimate only half of the EGI vectors and the other half of the polygon is obtained by simply flipping (reversing) the EGI vectors.

Since the underlying planar convex body K is origin symmetric, the linear algorithm based on (3.19) is equivalent to that of Prince and Willsky [37] described in Section 3.1.1 for reconstruction from support function measurements. Indeed, under the constraints for origin symmetry, the objective functions and feasible sets for the two optimization problems (3.2) and (3.17) are the same. However, in higher dimensions the corresponding problems are completely different.

3.3 Post-Processing Operation

The algorithm using (3.2),(3.17) and (3.19) constructs a polygon $\hat{\mathbf{z}}$ whose edges number up to twice the number of brightness function measurements (up to because some of the optimal edge lengths may be zero.) This may instigate huge storage requirements particularly for large M. Therefore, there may be a need for an extra operation to prune the number of edges of $\hat{\mathbf{z}}$ down to R (a user-defined value) and obtain an R-sided output polygon $\mathbf{z_{out}}$. The key challenge is to achieve this while retaining the overall shape. We have studied three approaches, namely, thresholding, clustering [5] (suggested to us by Gil Kalai), and decimation [44].

In *thresholding*, we discard edges with lengths smaller than a preset value and similarly discard vertices if the difference between the normal directions of its adjacent sides is less than another preset value. The thresholds are chosen arbitrarily and hence this method is rather ad hoc. Besides, it is not possible to ensure that the output polygon will have exactly R vertices.

Clustering is a more systematic method whereby the set of vertices are partitioned into a fixed number of R disjoint groups (clusters);[5] and [19]. The output polygon can be obtained by choosing a representative element from each cluster. We have chosen to use agglomerative hierarchical clustering which is a bottom-up clustering methodology. We start by assigning the individual elements to a separate cluster. We then evaluate the all-pair distance between the clusters using a suitable distance metric. The pair of clusters with the shortest distance are merged to form new cluster and the distances between the latter and all other clusters is calculated. The above process is repeated until we are finally left with R clusters. The representative element of a cluster is calculated as the mean of all the vertices belonging to that cluster.

Decimation is commonly used in the graphics community to simplify triangular and polygonal meshes [44]. We use an adapted version suitable for simplifying planar shapes. The procedure is outlined below.

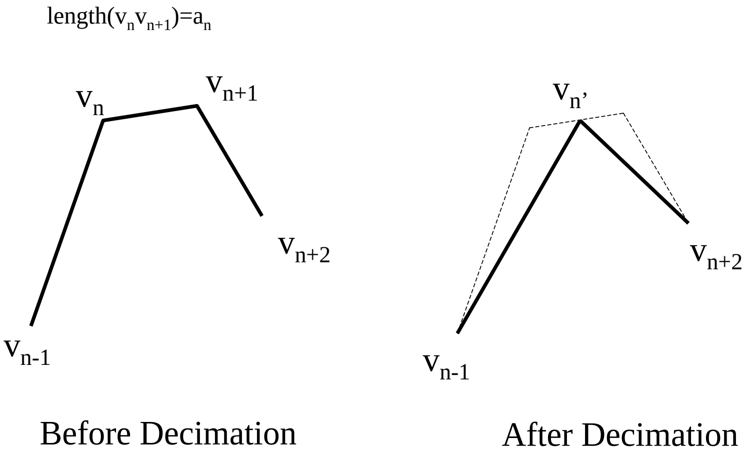

Figure 3.1: An intermediate step for decimation.

1. Form a priority queue using the edges of the polygon as the key with the maximum priority assigned to the smallest edge.

2. Choose the EGI vector $a_n u_n$ corresponding to the edge with the highest priority. Let v_n and v_{n+1} be two adjacent vertices which define the above edge.

3. Define a new vertex $v_{n'}$ given by $v_{n'} = \frac{(v_n + v_{n+1})}{2}$ and connect it to the adjacent vertices v_{n-1} and v_{n+2} to obtain the edges $v_{n-1}v_{n'}$ and $v_{n'}v_{n+2}$. Thus we have succeeded in decimating one edge.

4. Repeat the above steps until we obtain an R sided polygon.

Thus, by employing the algorithms outlined in this section, we can obtain the EGI of the polygon using corrupted support and brightness function measurements.

Chapter 4

Experimental results

The quality of the reconstructed polygon obtained using the algorithms outlined in the earlier chapter depend on experimental parameters like noise strength, eccentricity, scale, viewing set, etc. In this chapter, we use Monte-Carlo simulation results to study the behavior of our algorithms with respect to changes in these parameters.

We also require a shape comparison metric to quantify the quality of the reconstructed shapes. A survey of various shape matching metrics can be obtained in [42]. We employ two commonly used metrics, namely, the Hausdorff distance (δ_H) and the Symmetric Difference of Area (S).

The Hausdorff distance between two convex bodies K and L is

$$\delta_H(K, L) = \|h_K(\theta) - h_L(\theta)\|_\infty, \tag{4.1}$$

where h_K and h_L are the support functions of K and L respectively, and $\|\cdot\|_\infty$ is the infinity norm defined as,

$$\|\mathbf{x}\|_\infty = \max_i |x_i|.$$

The Symmetric Difference of Area between two bodies A and B centered at the origin can be defined as,

$$S(\mathrm{A}, \mathrm{B}) = area((\mathrm{A} - \mathrm{B}) \cup (\mathrm{B} - \mathrm{A})) \tag{4.2}$$

In other words it is the area of the non-overlapping regions of the two shapes (for more details see [15] where a relation between δ_H and S can also be obtained).

4.1 Sample reconstruction for shape from support-type functions

Here we present a few sample reconstructions obtained using the algorithms discussed in the earlier chapter.

4.1.1 Support Functions

Fig. 4.1 demonstrates the reconstructed polygons from support functions obtained by employing all three algorithms, namely, the non-linear algorithm (3.12) and the two previously proposed algorithms (3.2) and (3.7). All the algorithms were run under their required assumptions. The underlying shape is a user-defined quadrilateral having barycenter of its vertices at the origin, $\sigma = 0.1$, and the support data is measured from 18 equally spaced viewing directions in the range $[0, 2\pi]$ (Here and below, the entire interval, $[0, 2\pi]$ in this case, is divided into M bins of equal size and measurement vectors are positioned at the center of each bin.) The quality of shape reconstruction is compared by calculating the *Hausdorff distance* between the input and the output polygons.

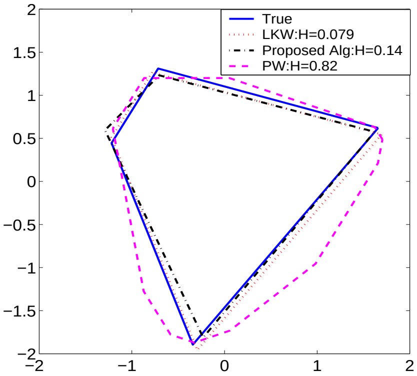

Figure 4.1: Shape from support function measurements.

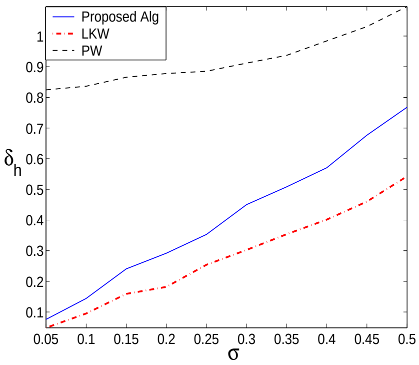

Figure 4.2: Simulation results for comparing support function algorithms.

Unlike the Prince-Willsky's algorithm (PW) where the normals are fixed along the viewing directions and the Lele, Kulkarni, Willsky algorithm (LKW) where the normals are pre-specified, the proposed non-linear algorithm estimates both normals and length of edges together such that the cost function in (3.12) is minimized. As seen from Fig. 4.1, the proposed algorithm does a good job compared to Lele, et al algorithm especially considering the fact that we use a much weaker prior information. This is further evident from Fig. 4.2 where we compare the performance of the above three algorithms. For each value of σ, the experiment is repeated 1000 times (Monte-Carlo simulations) and $\delta_h(\mathbf{z}, \hat{\mathbf{z}})$ was calculated each time. The mean of these values is plotted to obtain Fig. 4.2.

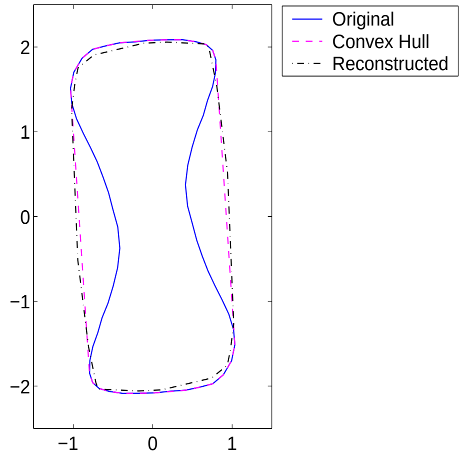

Figure 4.3: A non-convex body estimated using brightness functions.

4.1.2 Brightness Functions

The underlying body in Fig. 4.3 is non-convex and the brightness function values were measured from 36 equally spaced angles in $[0, \pi]$ and $\sigma = 0.2$. The estimated shape $\hat{\mathbf{z}}$ obtained using (3.17) is an origin symmetric polygon which closely approximates the convex-hull of the underlying body as demonstrated in the figure.

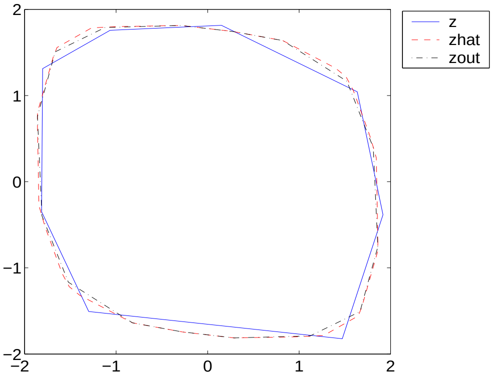

Figure 4.4: Shape from brightness values

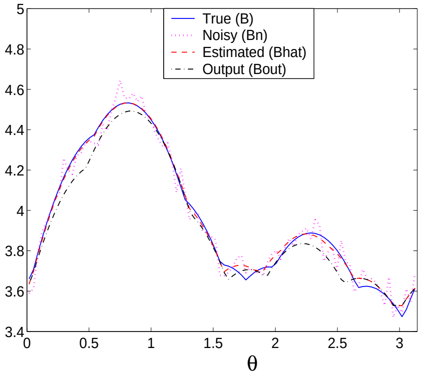

Figure 4.5: Brightness values.

The underlying shape in Fig. 4.4 is a user-defined octagon and brightness function were measured from 90 equally spaced viewing directions in $[0, \pi]$ and $\sigma = 0.05$. The estimated polygon $\hat{\mathbf{z}}$ is a 38-sided origin-symmetric polygon obtained using (3.17). The output polygon $\mathbf{z_{out}}$ was obtained from $\hat{\mathbf{z}}$ by pruning the number of sides down to 16 using decimation. Fig. 4.5 illustrates the true, noisy, estimated and output brightness function values.

4.2 Effect of experimental parameters

We now analyze the effect of experimental parameters on the quality of reconstruction using Monte-Carlo simulation runs.

4.2.1 Noise strength

The graph in Fig. 4.6 illustrates the behavior of $\delta_h(\mathbf{z}, \hat{\mathbf{z}})$ versus σ. $\mathbf{z}$ is a 15-sided regular polygon with eccentricity $= 1$ where eccentricity $\in (0, 1]$ is defined as the ratio of the minor axis to the major axis of an ellipse inscribing the polygon (a circle has eccentricity=1). The scale of the polygon (radius of the inscribing polygon) $\mathbf{z}$ is equal to 3 and the brightness function was measured from 36 equally spaced viewing directions in $[0, \pi]$. For each value of σ, the experiment is repeated 1000 times (Monte-Carlo simulations) and $\delta_h(\mathbf{z}, \hat{\mathbf{z}})$ is calculated each time. The mean of these values ($\bar{h}$) is plotted in Fig. 4.6 along with the $\pm\sigma_{\bar{h}}$ vertical error bars ($\sigma_{\bar{h}}$ is the standard error of the mean $\bar{h}$). We observe that if the noise power increases, the hausdorff distance between the input and estimated polygon increases and hence the estimation deteriorates.

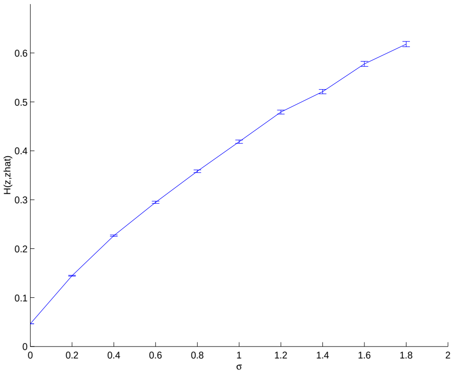

Figure 4.6: Effect of noise power

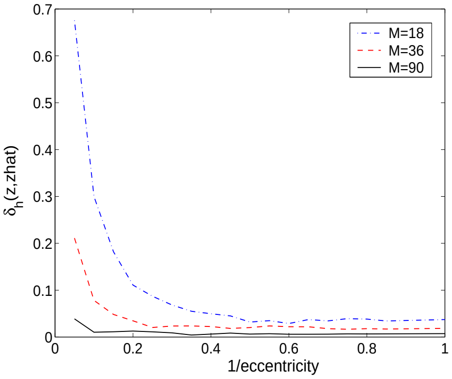

Figure 4.7: Effect of eccentricity

4.2.2 Eccentricity

The graph in Fig. 4.7 illustrates the behavior of our linear algorithm (3.17) as the eccentricity of the underlying affinely regular polygon changes. Here $K = 16$, $\sigma = 0$, and scale=1. The figure is composed of three graphs corresponding to three viewing sets consisting of 18, 36 and 90 equally spaced observation angles respectively. The error is very small for higher eccentric bodies indicating that it is much easier to estimate them compared to those with smaller eccentricity. Also note that the dense viewing set (90 observations) yields better results than the sparse viewing set (18 measurements) which can be attributed to the simple fact that more number of observations provide more information thereby implying better estimates.

4.2.3 Scale

The underlying polygon in Fig. 4.8 is a 12-sided regular polygon and the brightness values were measured from 36 equally spaced viewing directions in $[0, \pi]$. The scale of the underlying polygon is varied and the Hausdorff error is calculated using 500 Monte-Carlo simulations. The figure displays the graphs under two cases corresponding to $\sigma = 0.05$ and $\sigma = 0.1$ respectively. We infer that if the scale of the underlying polygon increases (i.e. polygon grows larger in size), the hausdorff error also increases.

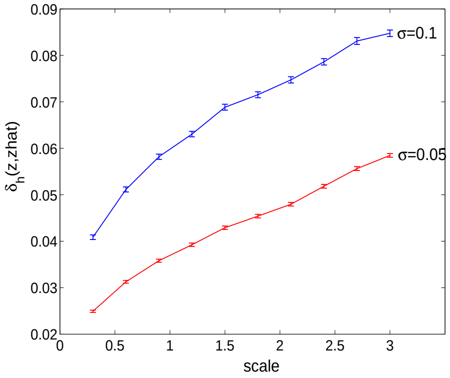

Figure 4.8: Effect of the scale of the underlying polygon.

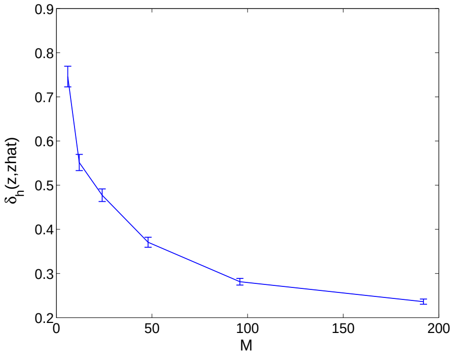

Figure 4.9: Effect of the the number of observations.

4.2.4 Number of measurements (Convergence)

Fig. 4.9 illustrates the effect of increasing the density of viewing set on the hausdorff distance $\delta_H(\mathbf{z}, \hat{\mathbf{z}})$. The underlying polygon is a 12-sided regular polygon with eccentricity = 1, scale = 3, noise strength $\sigma = 0.1$ and the graph was obtained using 100 Monte-Carlo runs. We observe that the hausdorff error exponentially decays as the number of measurements M increases. In the forthcoming work [8], it will be rigorously proved that the proposed algorithms converge with noisy data.

4.2.5 Comparison of post-processing operations

We compare performances of the two post-processing operations decimation and clustering in Fig. 4.10 where the underlying polygon is a 12-sided regular polygon with eccentricity=1, scale=1, $\sigma = 0.05$, and the brightness functions were measured from 36 equally spaced viewing directions in the range $[0, \pi]$. The estimated polygon $\hat{\mathbf{z}}$ obtained using (3.17) can have up to 72 sides which was fed as input to the post-processing routines clustering and decimation and a 12-sided output polygon $\mathbf{z_{out}}$ was obtained in both cases. We observe that decimation leads to lower errors and hence performs better than clustering.

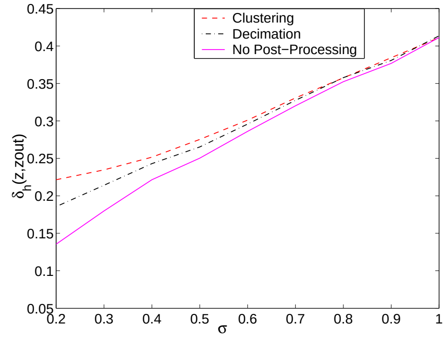

Figure 4.10: Comparing Post-Processing Operations.

Chapter 5

Statistical analysis using CRLB and confidence regions

In this chapter we present statistical analysis of the problem by employing the Cramer-Rao lower bound analysis and the confidence region visualization technique. Confidence regions quantitate and conveniently display the dependence of the experimental parameters like eccentricity, noise, viewing set, etc on the quality of the estimated shape thereby providing a more intuitive and elaborative understanding.

5.1 The (unconstrained) Cramer-Rao lower bound

The Cramér-Rao lower bound (CRLB) is a statistical tool often used in the performance evaluation of estimation problems. It provides the theoretical lower bound on the variance of any unbiased estimator; see, for example, [23, pp. 27–35]. Since no unbiased estimator can have lower variance than the CRLB, it provides a benchmark for comparison in the performance of an algorithm. Consider an observation vector $\mathbf{x}$

given by

$$\mathbf{x} = \mathbf{f}(\boldsymbol{\Psi}) + \mathbf{w} \tag{5.1}$$

where $\boldsymbol{\Psi} = [\psi_1, \ldots, \psi_P]^T$ is the vector of parameters to be estimated and $\mathbf{w}$ is the noise. The CRLB (see [23, pp. 30–44]) states that the covariance matrix is bounded below as follows:

$$\mathrm{Cov}(\hat{\boldsymbol{\Psi}}) \geq \mathbf{J}^{-1}(\boldsymbol{\Psi}). \tag{5.2}$$

Here $\hat{\boldsymbol{\Psi}}$ is the vector of estimated parameters and $\mathbf{J}(\boldsymbol{\Psi})$ is a $P \times P$ matrix called the Fisher information matrix (FIM), whose entries are given by the following expression involving the probability density function (p.d.f.) $p(\mathbf{x}; \boldsymbol{\Psi})$ of the observed data:

$$\mathbf{J}(i,j) = [\mathbf{J}(\boldsymbol{\Psi})]_{ij} = -E\left(\frac{\partial^2 \ln p(\mathbf{x}; \boldsymbol{\Psi})}{\partial \psi_i \partial \psi_j}\right), \tag{5.3}$$

for $i, j = 1, \ldots, P$, and where $E(.)$ denotes the expected value.

We first apply this bound to the problem of reconstructing from noisy support functions modelled by (3.11), with assumptions needed to derive (3.12). Therefore, this analysis is valid if the underlying polygon has barycenter of vertices at the origin and the correspondence t_m for every viewing direction is known. Recall that the noise is Gaussian with variance σ^2. The observation vector is $\mathbf{x} = [h(\alpha_1), \ldots, h(\alpha_M)]^T$ and the parameter vector is $\boldsymbol{\Psi} = [a_1, \ldots, a_N, \theta_1, \ldots, \theta_N]^T$, so that $P = 2N$. It follows from (3.8) that the joint p.d.f. for the support function data is

$$p_h(\mathbf{x}; \boldsymbol{\Psi}) = \prod_{m=1}^{M} \frac{1}{\sqrt{2\pi\sigma^2}} \exp\left[\frac{-1}{2\sigma^2}\left(h(\alpha_m) - \sum_{k=1}^{N} d_{t_m k} a_k \sin(\alpha_m - \theta_k)\right)^2\right]. \tag{5.4}$$

The FIM will be a $2N \times 2N$ matrix consisting of four $N \times N$ blocks $\mathbf{J_1}$, $\mathbf{J_2}$, $\mathbf{J_3}$, and $\mathbf{J_4}$. Specifically, for $i, j = 1, \ldots, N$, we have

$$\begin{aligned} \mathbf{J_1}(i,j) &= \mathbf{J}(i,j) = -E\left(\frac{\partial^2 \ln p(\mathbf{x};\mathbf{\Psi})}{\partial a_i \partial a_j}\right) = \frac{1}{\sigma^2}\sum_{m=1}^{M} d_{t_m i} d_{t_m j} s_{m,i}\, s_{m,j}, && (5.5)\\ \mathbf{J_2}(i,j) &= \mathbf{J}(i,j+N) = -E\left(\frac{\partial^2 \ln p(\mathbf{x};\mathbf{\Psi})}{\partial a_i \partial \theta_j}\right) = -\frac{a_j}{\sigma^2}\sum_{m=1}^{M} d_{t_m i} d_{t_m j} s_{m,i}\, c_{m,j}, && (5.6)\\ \mathbf{J_3}(i,j) &= \mathbf{J}(i+N,j) = -E\left(\frac{\partial^2 \ln p(\mathbf{x};\mathbf{\Psi})}{\partial \theta_i \partial a_j}\right) = -\frac{a_i}{\sigma^2}\sum_{m=1}^{M} d_{t_m i} d_{t_m j} s_{m,j}\, c_{m,i}, && (5.7)\end{aligned}$$

and

$$\mathbf{J_4}(i,j) = \mathbf{J}(i+N,j+N) = -E\left(\frac{\partial^2 \ln p(\mathbf{x};\mathbf{\Psi})}{\partial \theta_i \partial \theta_j}\right) = \frac{a_i a_j}{\sigma^2}\sum_{m=1}^{M} d_{t_m i} d_{t_m j} c_{m,i}\, c_{m,j}, \tag{5.8}$$

where $c_{m,k} = \cos(\alpha_m - \theta_k)$ and $s_{m,k} = \sin(\alpha_m - \theta_k)$. For calculations, see Appendix A. Thus $\mathbf{J}$ is a function of both the EGI vector parameters and the set of measurement directions.

Next we apply this bound to the problem of reconstructing from noisy brightness functions modelled by (3.13). Here we need to calculate the CRLB for only half the number of parameters due to the origin symmetry of the reconstruction. The observation vector $\mathbf{x} = [b(\alpha_1), \ldots, b(\alpha_M)]^T$ and the reduced space parameter vector is $\mathbf{\Psi} = [a_1, \ldots, a_{N/2}, \theta_1, \ldots, \theta_{N/2}]^T$, so that $P = N$. Using (2.32), (3.13) and under the Gaussian noise assumption, the joint p.d.f. for the brightness function data is

$$p_b(\mathbf{x};\mathbf{\Psi}) = \prod_{m=1}^{M} \frac{1}{\sqrt{2\pi\sigma^2}} \exp\left[\frac{-1}{2\sigma^2}\left(b(\alpha_m) - \sum_{k=1}^{N/2} a_k |\cos(\alpha_m - \theta_k)|\right)^2\right] \tag{5.9}$$

and the FIM is an $N \times N$ matrix consisting of four $N/2 \times N/2$ blocks we will again label $\mathbf{J_1}$, $\mathbf{J_2}$, $\mathbf{J_3}$, and $\mathbf{J_4}$. Specifically, for $i, j = 1, \ldots, N/2$, we have

$$\begin{aligned}
\mathbf{J_1}(i,j) &= \mathbf{J}(i,j) = -E\left(\frac{\partial^2 \ln p(\mathbf{x};\mathbf{\Psi})}{\partial a_i \partial a_j}\right) = \frac{1}{\sigma^2}\sum_{m=1}^{M} |c_{m,i}|\,|c_{m,j}|, && (5.10)\\
\mathbf{J_2}(i,j) &= \mathbf{J}(i,j+N/2) = -E\left(\frac{\partial^2 \ln p(\mathbf{x};\mathbf{\Psi})}{\partial a_i \partial \theta_j}\right), \\
&\qquad = \frac{a_j}{\sigma^2}\sum_{m=1}^{M} |c_{m,i}|\, s_{m,j}\,\mathrm{sgn}(c_{m,j}), && (5.11)\\
\mathbf{J_3}(i,j) &= \mathbf{J}(i+N/2,j) = -E\left(\frac{\partial^2 \ln p(\mathbf{x};\mathbf{\Psi})}{\partial \theta_i \partial a_j}\right), \\
&\qquad = \frac{a_i}{\sigma^2}\sum_{m=1}^{M} |c_{m,j}|\, s_{m,i}\,\mathrm{sgn}(c_{m,i}), && (5.12)
\end{aligned}$$

and

$$\begin{aligned}
\mathbf{J_4}(i,j) &= \mathbf{J}(i+N/2,j+N/2) = -E\left(\frac{\partial^2 \ln p(\mathbf{x};\mathbf{\Psi})}{\partial \theta_i \partial \theta_j}\right) \\
&\qquad = \frac{a_i a_j}{\sigma^2}\sum_{m=1}^{M} s_{m,i}\, s_{m,j}\,\mathrm{sgn}(c_{m,i})\,\mathrm{sgn}(c_{m,j}), && (5.13)
\end{aligned}$$

where $c_{m,k} = \cos(\alpha_m - \theta_k)$, $s_{m,k} = \sin(\alpha_m - \theta_k)$, and $\mathrm{sgn}(f)$ returns +1 or -1 according to whether f takes positive or negative values, respectively. For calculations, see Appendix A.

For brightness function measurements, the lower bound on the variance of the estimated shape parameters for any input polygon can be obtained from (5.2) and the inverse of the FIM from (5.10)–(5.13). The covariance matrix is an $N \times N$ matrix and consists of 4 blocks each of size $N/2 \times N/2$ as shown in (5.14).

$$\mathbf{Cov}([a_1, \ldots, a_{N/2}, \theta_1, \ldots, \theta_{N/2}]^T) = \begin{bmatrix} \mathbf{C_1} & \mathbf{C_2} \\ \mathbf{C_3} & \mathbf{C_4} \end{bmatrix} \qquad (5.14)$$

Using the origin symmetry property of the polygon, we can obtain the covariance matrix of the complete parameter space $[a_1, \ldots, a_N, \theta_1, \ldots, \theta_N]^T$ from (5.14) by simple replication as shown in (5.15).

$$\mathbf{Cov}([a_1, \ldots, a_N, \theta_1, \ldots, \theta_N]^T) = \begin{bmatrix} \mathbf{C_1} & \mathbf{C_1} & \mathbf{C_2} & \mathbf{C_2} \\ \mathbf{C_1} & \mathbf{C_1} & \mathbf{C_2} & \mathbf{C_2} \\ \mathbf{C_3} & \mathbf{C_3} & \mathbf{C_4} & \mathbf{C_4} \\ \mathbf{C_3} & \mathbf{C_3} & \mathbf{C_4} & \mathbf{C_4} \end{bmatrix} \tag{5.15}$$

Thus, the lower bound on the covariance of the EGI parameters estimated using brightness function measurements for a planar body is given by (5.15).

Similarly, for support function measurements, the lower bound on the estimated parameter vector $[a_1, \ldots, a_N, \theta_1, \ldots, \theta_N]^T$ can be calculated from (5.2) and the inverse of the FIM given by (5.5)–(5.8). However, in this case, the FIM turns out to be singular with rank $(2N - 2)$, yielding an infinite lower bound. The reason for this behavior is that the equality constraint (2.9) from Minkowski's conditions has not been taken into account. For brightness function measurements, only the inequality constraint (2.8) comes into play, in view of the formulation in (3.19). Such inequality constraints induce open subsets in the parameter space without any isolated boundaries and so do not affect the CRLB; see [13] for more details. On the other hand, equality constraints can reduce the dimension of the parameter space and cannot be ignored in the calculations. The next section addresses this issue.

5.2 The constrained Cramér-Rao lower bound

In this section we use the results of Stoica and Ng [40] for a *constrained Cramér-Rao lower bound* (CCRLB) analysis with a singular FIM.

Let $\mathbf{g_i}(\mathbf{\Psi}) = 0$, $i = 1, \ldots, Q$, where $\mathbf{\Psi} \in \Re^P$ and $Q < P$, be equality constraints defined by continuously differentiable functions, and let $\mathbf{g}(\mathbf{\Psi}) = [\mathbf{g_1}(\mathbf{\Psi}), \ldots, \mathbf{g_Q}(\mathbf{\Psi})]^T$ be the corresponding constraint vector. The gradient matrix of $\mathbf{g}$ is a $Q \times P$ matrix defined by

$$\mathbf{G}(\mathbf{\Psi}) = \frac{\partial \mathbf{g}(\mathbf{\Psi})}{\partial \mathbf{\Psi}^T},$$

where $\mathbf{G}$ should have full rank. Let $\mathbf{U} \in \Re^{P \times (P-Q)}$ be an orthogonal matrix in the null space of $\mathbf{G}(\mathbf{\Psi})$. Then

$$\mathbf{G}(\mathbf{\Psi})\mathbf{U} = 0.$$

The analysis in [40] shows that, under the given constraints, the covariance matrix of the estimated parameters should now satisfy,

$$\mathrm{Cov}(\hat{\mathbf{\Psi}}) \geq \mathbf{U}(\mathbf{U}^T\mathbf{J}\mathbf{U})^{-1}\mathbf{U}^T. \tag{5.16}$$

As seen from (5.16), the covariance matrix is obtained by projecting the singular fisher information matrix onto the constraint subspace.

Minkowski's condition introduces two equality constraints given by (2.9), and the gradient matrix of these constraints is the $2 \times 2N$ matrix

$$\mathbf{G}(\mathbf{\Psi}) = \begin{bmatrix} \cos\theta_1 & \cdots & \cos\theta_N & -a_1\sin\theta_1 & \cdots & -a_N\sin\theta_N \\ \sin\theta_1 & \cdots & \sin\theta_N & a_1\cos\theta_1 & \cdots & a_N\cos\theta_N \end{bmatrix}. \tag{5.17}$$

After carrying out the analysis discussed in this section and using (5.16) and (5.17), we will be able to obtain the CCRLB for the estimated parameters. To summarize, the lower bound on the variance of the estimated EGI parameters for brightness functions and support functions can be obtained using (5.15) and (5.16) respectively. However, our final aim is to reconstruct the 2-D shape from support-type function data and not simply to find its EGI. Thus what we really need is to find bounds with respect to the 2-D shape and not just the parameters. Rather than the quality of estimates of $\mathbf{\Psi}$, we need a global quality measure of the entire reconstructed boundary. This can be achieved by developing asymptotic confidence regions around the true shape, a topic introduced in the next section.

5.3 Confidence Region Analysis

5.3.1 Introduction

Asymptotic global confidence regions are used to analyze and visualize the performance of 2-dimensional parametric shape estimators. Assuming a maximum likelihood estimator (MLE) operating in the asymptotic regime, the CRLB for the shape parameters can be used to define a confidence region around the true boundary of the shape, as in [43]. Note that the MLE is asymptotically normal, unbiased and asymptotically attains the CRLB; see [23, pp. 164–167]. We follow [43] below; in our analysis to develop confidence regions.

Consider a 2-D shape parameterization of the form,

$$\mathbf{s}(t;\mathbf{\Psi}) = [s_x(t;\mathbf{\Psi}), s_y(t;\mathbf{\Psi})]^T,$$

where $\mathbf{s}$ is the boundary parameterized by $t \in [0, T]$, and s_x and s_y give the x and y coordinates. Here $\mathbf{\Psi} \in \Re^P$ is the P-dimensional parameter vector. At each point along the boundary (i.e., for all $t \in [0, T]$) we determine a local confidence region $U_\beta(t) \subset \Re^2$ centered at the true point $\mathbf{s}(t; \mathbf{\Psi})$ (see Fig. 5.1). The size of the local confidence region depends on β, which in turn depends on the chosen local confidence level $\eta \in [0, 1]$; if $\hat{\mathbf{s}}(t)$ is estimated using an MLE operating in the asymptotic regime, then

$$\Pr\{\hat{\mathbf{s}}(t) \in U_\beta(t)\} = \eta.$$

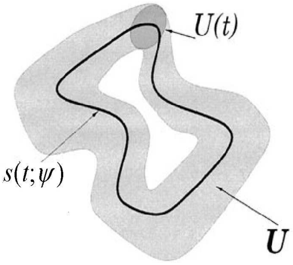

Figure 5.1: Local and global confidence regions (from [43]).

The first step towards generating the local confidence region for a point $\mathbf{s}(t; \mathbf{\Psi})$ on the boundary $\mathbf{s}$ is to calculate the CRLB ($\mathbf{C}_{\mathbf{\Psi}} = \mathrm{Cov}(\mathbf{\Psi}) \in \Re^{P \times P}$) of the 2-D shape parameters. From this we find the covariance matrix of $\mathbf{s}(t; \mathbf{\Psi})$; a 2×2 matrix defined as follows,

$$\mathbf{C}_{\mathbf{s}}(t) = \nabla_{\mathbf{\Psi}} \mathbf{s}(t; \mathbf{\Psi}) \mathbf{C}_{\mathbf{\Psi}} \left[\nabla_{\mathbf{\Psi}} \mathbf{s}(t; \mathbf{\Psi})\right]^T \tag{5.18}$$

where $\nabla_{\mathbf{\Psi}} \mathbf{s}(t; \mathbf{\Psi}) \in \Re^{2 \times P}$ is the gradient of $\mathbf{s}(t; \mathbf{\Psi})$ with respect to $\mathbf{\Psi}$. $\mathbf{C}_{\mathbf{s}}(t)$ gives the individual variances and the covariance between the x and y coordinates of any point on the shape boundary that is estimated using the MLE operating in the asymptotic regime. The smallest size local confidence region $U_\beta(t)$ for the point $\mathbf{s}(t)$ is given as,

$$U_\beta(t) = \{\mathbf{x} \in \Re^2 : (\mathbf{x} - \mathbf{s}(t))^T \mathbf{C_s}(t)^{-1}(\mathbf{x} - \mathbf{s}(t)) \le \beta^2\} \tag{5.19}$$

where $\beta > 0$ and β is calculated by assuming that the left-hand side of (5.19) is a Chi-squared random variable of degree 2 such that the probability that it is less than or equal to β^2 is η; i.e. $\Pr\{\chi_2^2 \le \beta^2 = \eta\}$. Note that the size of the local confidence region is directly proportional to the local confidence level η. For each t, $U_\beta(t)$ is an ellipse centered at $\mathbf{s}(t)$ and hence it is also referred to as local confidence ellipse. A global confidence region can now be obtained by moving $U_\beta(t)$ along the boundary,

$$U_\beta = \bigcup_{t \in [0,T]} U_\beta(t). \tag{5.20}$$

Asymptotic global confidence region defines an uncertainty band around the entire boundary of the true shape in which the estimated shape can lie (see Fig. 5.1) Another probability of interest is the global confidence level which is defined as,

$$\gamma = \Pr\{\hat{\mathbf{s}}(t) \in U_\beta, \forall t \in [0, T]\} \tag{5.21}$$

Thus global confidence level is the probability that the estimated shape $\hat{\mathbf{s}}$, lies completely inside the uncertainty band developed around the true shape.

5.3.2 Local confidence regions for support-type data

Once the EGI of the approximating polygon has been estimated from the support-type function measurements, we may use (2.18) to obtain

$$\mathbf{s}(t; \mathbf{\Psi}) = \left[\sum_{k=1}^{N} d_{tk} a_k \cos(\theta_k + \pi/2), \sum_{k=1}^{N} d_{tk} a_k \sin(\theta_k + \pi/2)\right]^T, \tag{5.22}$$

where the discrete values $t = 1, \ldots, N$ of t each index a vertex of the polygon. From this, we find the gradient $\nabla_{\mathbf{\Psi}} \mathbf{s}(t; \mathbf{\Psi}) \in \Re^{2\times 2N}$ to be,

$$\begin{bmatrix} d_{t1}\cos(\theta_1+\pi/2) & \cdots & d_{tN}\cos(\theta_N+\pi/2) & -d_{t1}a_1\sin(\theta_1+\pi/2 & \cdots & -d_{tN}a_N\sin(\theta_N+\pi/2) \\ d_{t1}\sin(\theta_1+\pi/2) & \cdots & d_{tN}\sin(\theta_N+\pi/2) & d_{t1}a_1\cos(\theta_1+\pi/2) & \cdots & d_{tN}a_N\cos(\theta_N+\pi/2) \end{bmatrix}. \tag{5.23}$$

Using (5.18), (5.19), and (5.23), the asymptotic local confidence ellipses $U_\beta(t)$ can be calculated for $t = 1, \ldots, N$.

In the case of support function measurements, the matrix $\mathbf{C}_{\mathbf{\Psi}}$ in (5.18) is substituted by the CCRLB given by the right-hand side of (5.16). For brightness functions measurements, we instead use the CRLB given by the right-hand side of (5.15). For an N-sided polygon, t varies discretely from $1, \ldots, N$ and therefore we obtain N local confidence regions each centered at its corresponding true vertex $\mathbf{s_t}$.

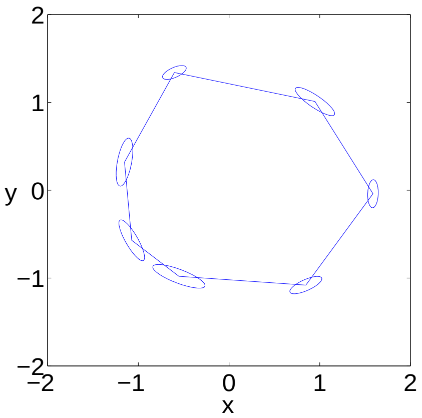

Figure 5.2: Local confidence regions for shape from support function.

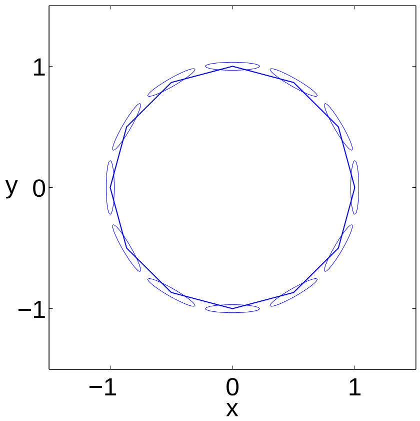

Figure 5.3: Local confidence regions for shape from brightness function.

Fig. 5.2 shows the local confidence ellipses for a polygon with $N = 7$ sides whose support function is measured at $M = 180$ equally spaced angles. The noise is Gaussian with $\sigma = 0.2$ and the local confidence level is η=0.73. From (2.28) we know that each measurement at an angle α_m lying between adjacent outer normal angles θ_t and θ_{t+1} will depend only on the position of the vertex of the polygon between these two angles. Therefore the greater the size of the interval $[\theta_t, \theta_{t+1}]$, the more information we have about the corresponding vertex of the polygon and the smaller the local confidence ellipse will be. This is verified by Fig. 5.2.

Fig. 5.3 illustrates the local confidence ellipses for an origin-symmetric, regular polygon with $N = 12$ sides whose brightness function is measured from $M = 36$ equally spaced viewing angles in the range $[0, \pi]$. The noise is Gaussian with $\sigma = 0.1$ and the local confidence level is η=0.73. Note that the local confidence ellipses are all congruent which implies that there is the same amount of uncertainty associated with each vertex. The reason is that the underlying polygon is a regular polygon having eccentricity = 1. Because of the circular shape and equally spaced set of viewing directions, it is equally hard to estimate each vertex and hence all the local confidence ellipses are of the same size.

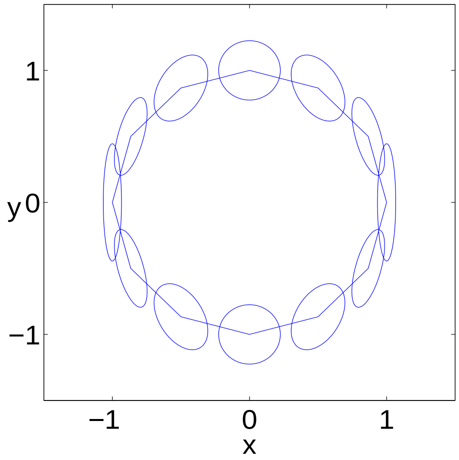

Figure 5.4: Confidence regions for a regular polygon obtained using (2.10).

If we use the vertex reconstruction method given by (2.10) instead of (2.18) while defining $\mathbf{s}(t;\mathbf{\Psi})$ in (5.22), the local confidence ellipses in Fig. 5.3 instead look like as shown in Fig. 5.4. Note that the size of the local confidence ellipses increase with the index t which can be attributed to the unequal error distribution given by (2.26). The confidence regions in Fig. 5.4 effectively display that (2.10) is a poor method to obtain shape from EGI.

5.3.3 Effect of experimental parameters on the confidence regions

We now proceed to study the effect of various experimental parameters on the confidence regions for shape from support type functions.

Noise Power: Increasing the noise corrupting the support-type measurements decreases the signal to noise ratio (SNR) and leads to bad estimates. Fig. 5.5 and Fig. 5.6 are obtained using the same shape and parameters as in Fig. 5.2 and Fig. 5.3 respectively, except that the noise strength σ was increased to 0.3 for the support case and 0.2 for the brightness case. We observe that the size of local confidence ellipses has increased and therefore the associated uncertainty is higher making the estimation process difficult. An opposite effect is observed if the noise strength is decreased.

Effect of the number of measurements: Increasing the number of measurements provides more information about the shape which lead to better shape estimation. Fig. 5.8 is obtained using the same shape and parameters as in Fig. 5.3 except that the number of brightness function measurements is increased from 36 to 90. We

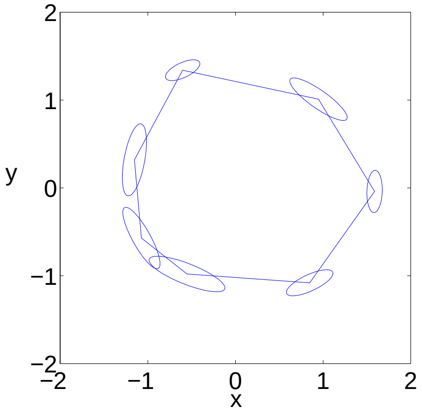

Figure 5.5: Effect of noise power on local confidence ellipses for support functions data.

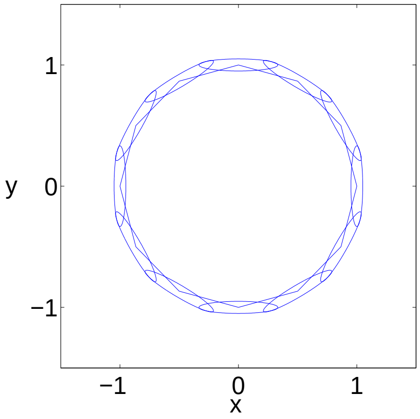

Figure 5.6: Effect of noise power on local confidence ellipses for brightness functions.

observe that the confidence ellipses have grown smaller in size indicating that the uncertainty has decreased. Thus we get better shape estimates by increasing the number of measurements. An opposite effect is observed by decreasing the number of measurements as evident from Fig. 5.7 which was obtained using 72 equally spaced viewing directions instead of 180 with the remaining parameters similar to Fig. 5.2.

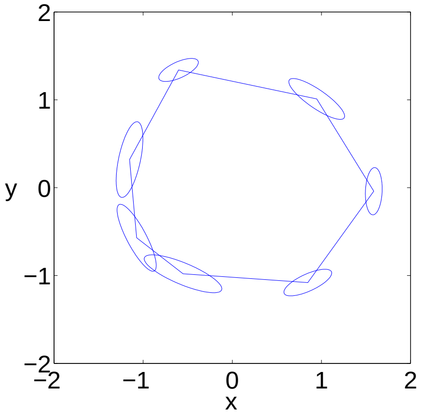

Figure 5.7: Local confidence ellipses for support function with higher number of measurements.

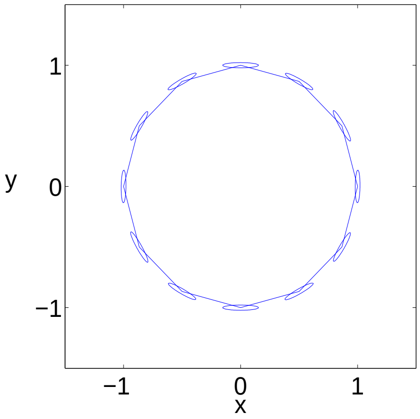

Figure 5.8: Local confidence ellipses for brightness function with fewer measurements.

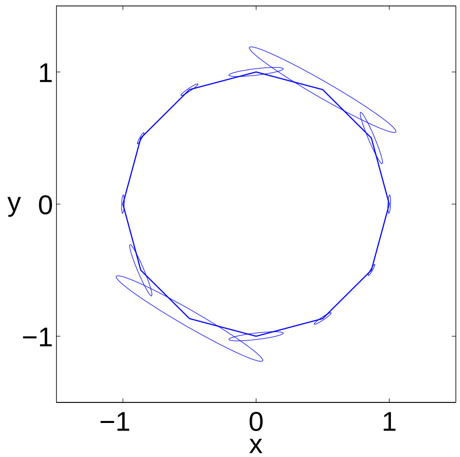

Figure 5.9: Measurement angles sampled from Von-Mises distribution

Randomly drawn viewing set: In Fig. 5.6, the underlying polygon and parameters are as in Fig. 5.3, but the $M = 1000$ measurement angles are randomly drawn from the von Mises distribution $V(\pi/3, 5)$ (see [34]) with mean $\pi/3$ and concentration parameter $\kappa = 5$. The high value of κ leads to a very heavy concentration of measurement angles near $\pi/3$. A brightness function measurement provides the greatest information about the vertices of the polygon contained in the support lines parallel to the measurement direction. This explains the very different sizes of the local confidence ellipses in Fig. 5.6, which are largest at the vertices that lie in support lines parallel to the relatively few measurement directions orthogonal to $\pi/3$.

Effect of eccentricity Fig. 5.10 is obtained using an affinely regular polygon with $N = 8$ sides whose support function is measured at $M = 72$ equally spaced angles, with $\sigma = 0.1$. The local confidence ellipses vary in size, the largest occurring at vertices 1 and 5 where the "curvature" is smallest. This is compatible with earlier

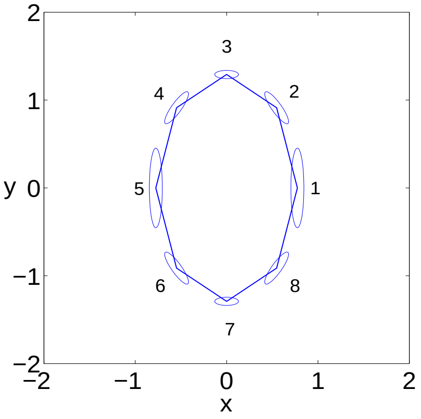

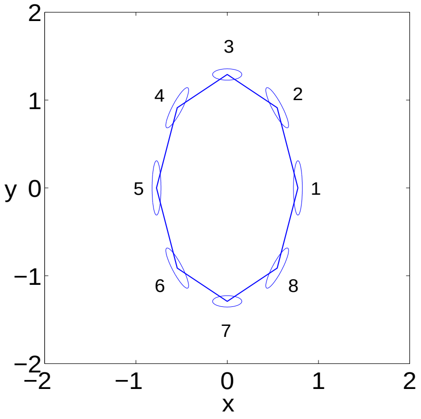

Figure 5.10: Local confidence regions for an affinely regular polygon with equally spaced measurement directions.

Figure 5.11: Local confidence regions for an affinely regular polygon with a better set of viewing directions.

remarks. If the user has prior information about the eccentricity of the input polygon, the distribution of the measurement angles can be changed accordingly to compensate. This is demonstrated in Fig. 5.11, where a total of 72 measurements are made in 12 equally spaced directions each in the intervals $[0, \pi/6)$, $[\pi/6, 5\pi/6)$ and $[5\pi/6, \pi)$, and the 36 antipodal directions. The local confidence ellipse have become more nearly equal in size.

5.3.4 Global Confidence Region

From the discussion in the previous subsection, we can only develop the local confidence region for the vertices of the polygon. In this case the global confidence region U_β as defined in (5.20) will not give us an uncertainty band around the entire shape. Moreover, we are not able to find the local confidence region for any point on the boundary of the polygon; as we are restricted to the vertices. The motivation behind this sub-section is to enable us to find the confidence region for any point on the shape boundary thereby giving us the global confidence region which will be in the form of a continuous uncertainty band completely enclosing the true shape as in Fig. 5.1.

We are restricted to the confidence regions of only the vertices because t in (5.22) takes on discrete values in the interval $[1, N]$ with each value of t indexing a vertex of the polygon. Let us define a shape parameter τ which can take continuous values in the interval $[1, N+1]$. The new shape parameterization $\mathbf{s}(\tau, \mathbf{\Psi})$ can be obtained as follows,

$$\mathbf{s}(\tau; \mathbf{\Psi}) = (\lceil \tau \rceil - \tau)\mathbf{s}(\lfloor \tau \rfloor; \mathbf{\Psi}) + (\tau - \lfloor \tau \rfloor)\mathbf{s}(\lceil \tau \rceil; \mathbf{\Psi}) \tag{5.24}$$

where $\lfloor \tau \rfloor$ = floor(τ) i.e. rounding τ towards the direction of negative infinity, and $\lceil \tau \rceil$ = ceil(τ) i.e. rounding τ towards the direction of positive infinity. Note that $\tau = 1$ and $\tau = N+1$ refer to the same point on the polygon boundary. Using (5.22) and substituting $t = \lfloor \tau \rfloor$ we get,

$$\mathbf{s}(\lfloor \tau \rfloor; \mathbf{\Psi}) = \left[\sum_{k=1}^{N} d_{\lfloor \tau \rfloor}(k) a_k \cos(\theta_k + \pi/2), \sum_{k=1}^{N} d_{\lfloor \tau \rfloor}(k) a_k \sin(\theta_k + \pi/2) \right] \tag{5.25}$$

Similarly using (5.22) and substituting $t = \lceil \tau \rceil$ we get,

$$\mathbf{s}(\lceil \tau \rceil; \mathbf{\Psi}) = \left[\sum_{k=1}^{N} d_{\lceil \tau \rceil}(k) a_k \cos(\theta_k + \pi/2), \sum_{k=1}^{N} d_{\lceil \tau \rceil}(k) a_k \sin(\theta_k + \pi/2) \right] \tag{5.26}$$

Finally from (5.24),(5.25) and (5.26) we get,

$$\mathbf{s}(\tau; \mathbf{\Psi}) = \left[\sum_{k=1}^{N} q_{\tau k} a_k \cos(\theta_k + \pi/2), \sum_{k=1}^{N} q_{\tau k} a_k \sin(\theta_k + \pi/2) \right]^T, \tag{5.27}$$

for $1 \leq \tau \leq N+1$, where

$$q_{\tau k} = (\lceil \tau \rceil - \tau) d_{\lfloor \tau \rfloor k} + (\tau - \lfloor \tau \rfloor) d_{\lceil \tau \rceil k}.$$

We follow the confidence region analysis discussed earlier in this section using the new shape parameterization (5.27). Since τ can take continuous values in the interval $[1, N+1]$, we can obtain the local confidence region of any point on the boundary of the polygon and using (5.20) we can thus obtain the uncertainty band.

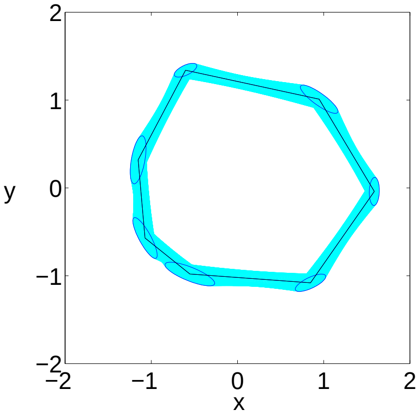

Figure 5.12: Global confidence region for support functions

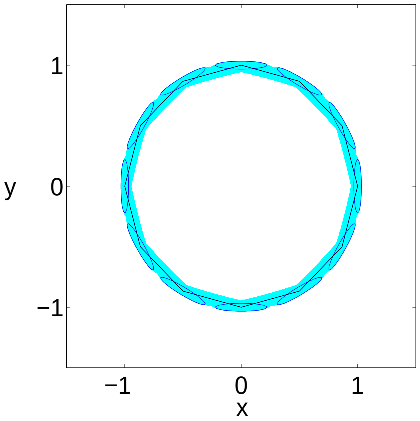

Figure 5.13: Global confidence region for brightness functions

Fig. 5.12 shows the global confidence region obtained using (5.27) for the same polygon as in Fig. 5.2. The continuous parameter τ was sampled at 0.005 i.e. we repeatedly generated the local confidence regions for the polygon with τ varying from 1 to 13 in steps of 0.005. The local confidence region of the vertices are highlighted in the figure for better illustration. Similarly, Fig. 5.13 shows the uncertainty band for the polygon in Fig. 5.3 with τ sampled at steps of 0.005.

Chapter 6

Performance analysis and further experimental results

In this chapter, we use confidence regions to carry out a statistical performance analysis of our proposed algorithms to find out how close we are to optimal. Later, we also present some experimental results demonstrating both the sample reconstructions and the uncertainty regions together.

6.1 Performance Analysis

The optimal algorithm is the MLE operating in the asymptotic regime, since it is normal, unbiased, and attains the CRLB. Though the algorithms we have considered above are not necessarily unbiased, their performance can be measured effectively by comparing them with the MLE operating in the asymptotic regime, using the confidence regions developed earlier for this algorithm. The performance analysis can be carried out with the aid of both local and global confidence regions as discussed below.

6.1.1 Local Confidence Regions

Here we carry out a performance analysis of the linear algorithms for brightness function (3.17) using local confidence regions.

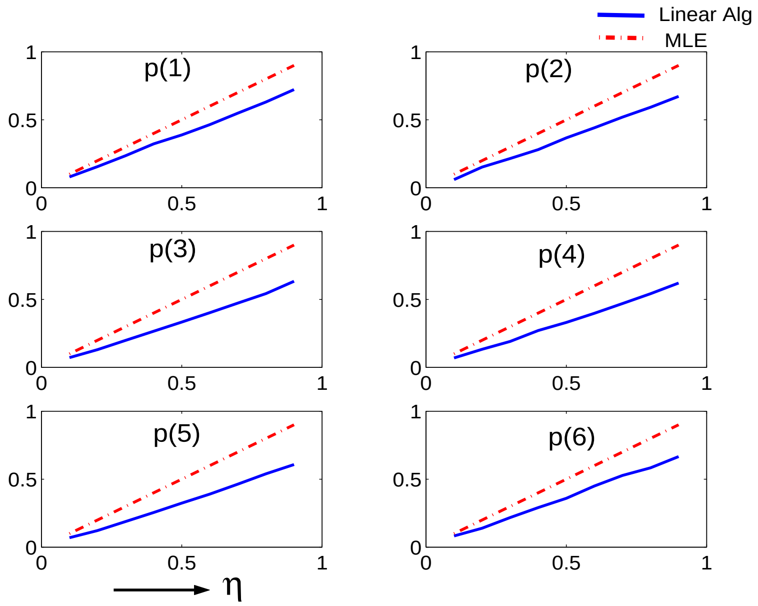

Figure 6.1: Performance evaluation using local confidence region for brightness functions for each vertex of the 12-sided polygon in Fig. 4.3

Let $\hat{\mathbf{s}}_{alg}$ be the estimated shape boundary obtained using our linear algorithm discussed in Section 3.2. For every vertex $\hat{\mathbf{s}}_{alg}(t; \mathbf{\Psi})$, $t = 1, \ldots, N$, we calculate the probability

$$p(t) = \Pr\{\hat{\mathbf{s}}_{alg}(t) \in U_\beta(t)\} \tag{6.1}$$

that it falls inside its corresponding local confidence region $U_\beta(t)$. Fig. 6.1 compares our linear algorithm with the MLE for the same polygon and parameters used in Fig. 5.3. Due to origin symmetry of the polygon, we do a performance analysis of only half of the number of vertices. We determine the local confidence ellipses associated with each of six vertices at values of η between 0 and 0.9. The probability $p(t)$ in (6.1) was calculated for each η at every vertex using 1000 instances of the reconstructed polygon $\hat{\mathbf{s}}_{alg}$ obtained by Monte-Carlo simulation. For an MLE operating in the asymptotic regime , the probability $p(t) = \eta$ (by definition), indicated by straight lines of slope 1 in each subplot of Fig. 6.1. We observe that the curve for the linear algorithm is below the MLE operating in the asymptotic regime implying that we are less likely to fall inside the confidence region.

6.1.2 Global Confidence Regions

Here we present a performance analysis for the algorithms from Chapter three, using global confidence regions. Let $\hat{\mathbf{s}}$ be the estimated shape boundary resulting from a given algorithm and define the corresponding error probability $e = e(\beta)$ by

$$e = 1 - \Pr\{\hat{\mathbf{s}} \in U_\beta\}. \tag{6.2}$$

Thus e is the probability that the estimated shape boundary $\hat{\mathbf{s}}$ does *not* lie completely inside the global confidence region U_β. By Monte Carlo simulation, we can compare performances of algorithms by plotting for each the error probability for a range of values of β. We use a log scale on the vertical axis for better illustration.

Fig. 6.2 provides a performance evaluation of the brightness function algorithms, based on 1000 runs of each algorithm for a regular polygon with $N = 10$ sides, $M = 45$ equally spaced measurement angles, and $\sigma = 0.04$. The graphs give the relative performance of the linear brightness function algorithm based on (3.19), the non-linear algorithm based on (3.14) (MLE (non-asymptotic)), and the MLE (asymp-

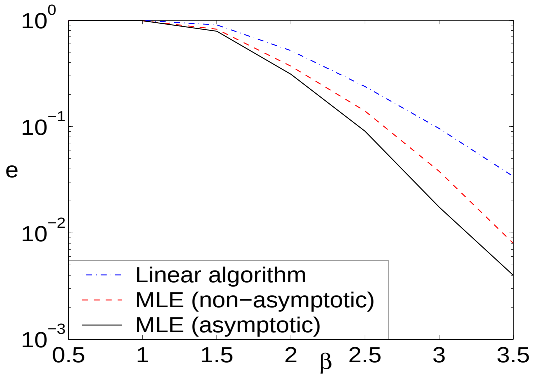

Figure 6.2: Performance evaluation of brightness function algorithms.

totic). The latter is produced as follows. Since the MLE is asymptotically normal, unbiased, and attains the CRLB, we first draw an EGI sample from the normal distribution $N(\mathbf{\Psi}, \mathbf{C}_{\mathbf{\Psi}})$ where the matrix $\mathbf{C}_{\mathbf{\Psi}}$ is is given by the right-hand side of (5.15). From the EGI sample we obtain the estimated boundary $\hat{\mathbf{s}}$ by (5.22), and the value of e in (6.2) is estimated from 1000 independent trials of this type. Fig. 6.2 indicates in particular that the linear brightness function algorithm does a reasonably good job when compared to the optimal MLE estimator.

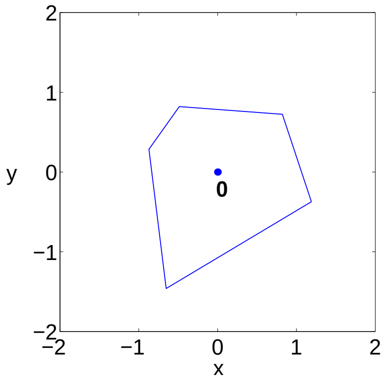

Figure 6.3: Underlying polygon used for the analysis in Fig. 6.4.

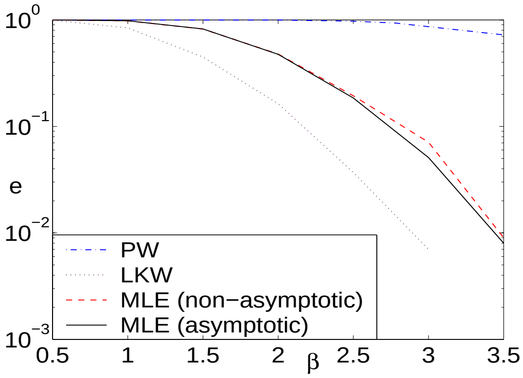

Figure 6.4: Performance evaluation of support function algorithms.

Fig. 6.4 provides a similar evaluation of the support function algorithms, based on 1000 runs of each algorithm for a polygon with $N = 5$ sides, $M = 72$ equally spaced measurement angles, and $\sigma = 0.1$. The underlying polygon has vertices with barycenter at $\mathbf{0}$ as shown in Fig. 6.3. The graphs in Fig. 6.4 give the relative performance of the algorithms of Prince and Willsky (PW), Lele, Kulkarni, and Willsky (LKW), the non-linear algorithm based on (3.12) (MLE (non-asymptotic)), and the MLE (asymptotic). However, we stress that the comparison is not really a fair one, since on the one hand the PW algorithm produces outputs with outer normals in the measurement directions, and on the other, the LKW algorithm assumes, as prior knowledge, *unknown* outer normal angles. In view of this it is hardly surprising that the PW algorithm performs much worse, and the KLW algorithm much better, than the MLE algorithms.

6.2 More Experimental Results

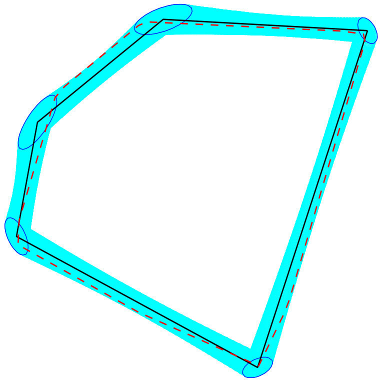

Figure 6.5: Shape from support function measurements.

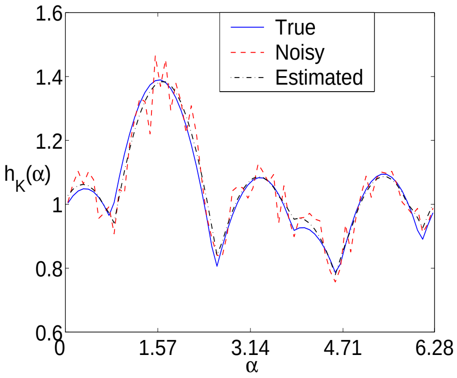

Figure 6.6: True, noisy, and estimated support function measurements.

Figs. 6.5 and 6.7 illustrate true (solid line) and estimated (dotted line) polygons resulting from the linear algorithms based on (3.2) and (3.19) using noisy support and brightness function measurements, respectively. In each case the noise level is $\sigma = 0.1$ and local and global confidence regions corresponding to local confidence level $\eta = 0.9$ are shown for comparison. For Fig. 6.5 the true polygon has $N = 8$ sides with support function measured at $M = 72$ equally spaced angles.

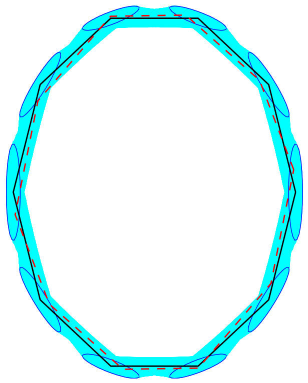

Figure 6.7: Shape from brightness function measurements.

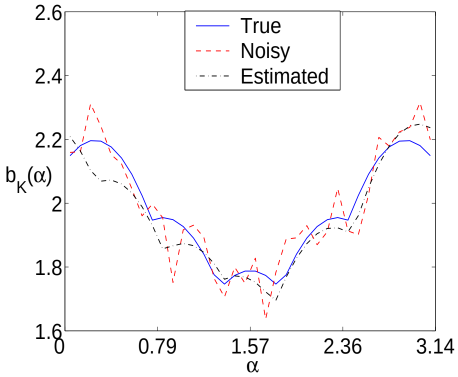

Figure 6.8: True, noisy, and estimated brightness function measurements.

The true polygon in Fig. 6.7 is an affinely regular polygon with $N = 10$ sides whose brightness function is measured at $M = 36$ equally spaced angles; the extra post-processing step of decimation described in Section 3.3 was used to prune the number of edges down to 10. Figs. 6.6 and 6.8 depict the true, noisy, and estimated measurements in each case.

6.3 3-D shape reconstruction from brightness functions

This section provides some illustrations of 3-D shape from brightness functions. This work was conducted by Richard Gardner and Peyman Milanfar (for a detailed discussion see [9] and [10]). They follow the same two step approach outlined in Fig. 1.2. The algorithms discussed in Section 3.2 for estimating EGI from noisy brightness values are valid and can be extended to the higher dimensions. However the second step comprising of estimating cartesian coordinates from noisy EGI is a challenging problem. Currently, they employ Little's algorithm [32] to estimate 3-D cartesian coordinates from pure EGI. However, the problem of shape for noisy EGI values has not been carefully studied in the past and forms a challenging area of future work. The code used to simulate the 3-D brightness function algorithms was provided by Richard Gardner and Chris Street.

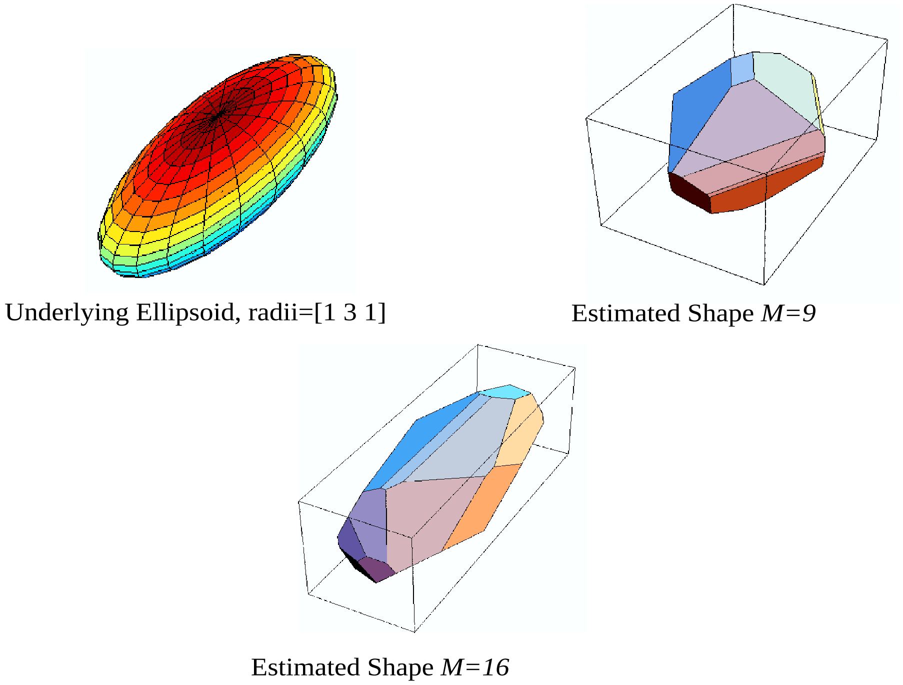

Underlying Ellipsoid, radii=[1 3 1]

Estimated Shape *M*=*9*

Estimated Shape *M*=*16*

Figure 6.9: 3-D shape reconstruction from brightness functions

The underlying polygon in Fig. 6.9 is an ellipsoid with radii $= [1, 3, 1]$. The input consisted of exact brightness function measurements along $M = 9$ and $M = 16$

viewing directions corresponding to the spherical polar angles

$$\left\{\left(\frac{2\pi r}{3}, \frac{\pi s}{3}\right) : r = 0, 1, 2, s = 0, 1, 2\right\} \tag{6.3}$$

and,

$$\left\{\left(\frac{2\pi r}{4}, \frac{\pi s}{4}\right) : r = 0, 1, 2, 3, s = 0, 1, 2, 3\right\} \tag{6.4}$$

respectively. Furthermore, the number of facets of the estimated polygon were reduced down to 30 using clustering as the post-processing operation. We observe that the output for $M = 16$ resembles the underlying polygon more closely than that for $M = 9$. Thus, as the number of brightness function measurements increase, the quality of reconstruction improves.

Chapter 7

Conclusions and future work

In this chapter, we introduce a new problem called shape reconstruction from “lightness functions”. We discuss future directions of research emanating from the current work and also provide conclusive remarks.

7.1 Lightness Functions

The brightness functions measurements obtained using model (2.31) are independent of the illumination of the body; the model does not incorporate the presence and effects of a light source. Imagine an object with lambertian surface that is so poorly resolved that its entire image falls on a single pixel at any given time. In this case, the only available information about the object is the time history of its tracked pixel intensity. If the object is rotating, then the time history is determined by two factors, namely the brightness function of the object and the illumination of the object in the direction in which it is exposed to the camera (see Fig. 7.1 for example). The measurement of this time history for an atmosphereless body is what astronomers refer to as the “lightcurve” of the object (see Fig. 7.2 and [11]) and the problem is to estimate the shape of the object using the weak information provided by the “lightcurves”. Clearly we need to extend the model in (2.31) to account for such practical scenarios.

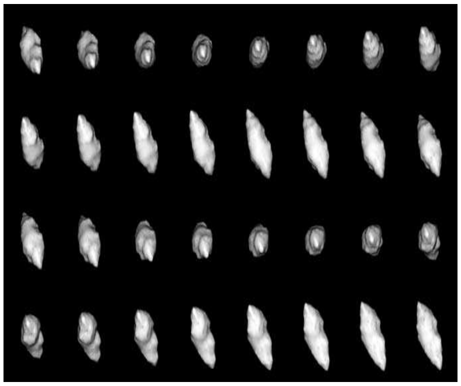

Figure 7.1: Images of a rotating asteroid from several viewpoints.

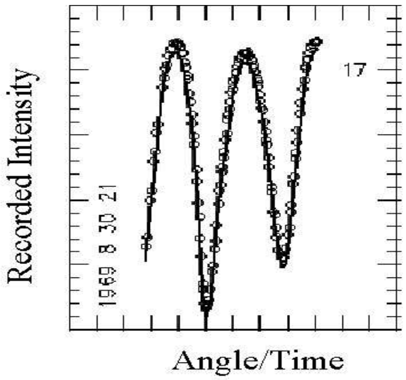

Figure 7.2: Lightcurves (from [11]).

We introduce the “lightness functions” which are defined for objects having lambertian surface that are illuminated by a light source. The light source is considered infinitely far away from the object it is illuminating and hence all the rays have a common direction (directional light source). Sunlight which illuminates astral bodies is a commonly cited example of a directional light source. The radiance of a lambertian reflector is the same from all viewing directions. Such a surface follow Lambert’s Cosine Law which states that the radiance from an element of area of a surface varies as the cosine of the angle between that direction and the perpendicular to the surface element.

$$\mathrm{L(P)} = \rho \cos \lambda \tag{7.1}$$

where, L(P) is the diffused reflectance from the surface, ρ is the effective albedo which is proportional to the intensity of the illuminant and the reflectance properties of the surface, and λ is the angle between the normal to the surface and the incoming light ray. Note that the brightness function model in (2.31) can also be written as

$$b(v) = \int_S f(u) \max(u^T v, 0) du \tag{7.2}$$

Using (7.1) and (7.2) we define the lightness function as,

$$l(v, w) = \int_S \rho(u) f(u) \text{max}(-u^T v, 0) \text{max}(u^T w, 0) du \tag{7.3}$$

Note that the lightness function is a function of the viewing direction v as well as the direction of the incoming light ray w. Moreover, unlike the brightness function, the periodicity interval is 2π. The lightness function is also a weaker form of data compared to brightness functions. Every point on the object boundary has to satisfy an additional condition given by the term $\max(u^T w, 0)$ which checks if the point is visible or not. Therefore, parts of the object that are not illuminated when observed from a particular viewing direction do not contribute towards the lightness function measurement.

Fig. 7.3 shows preliminary results for two cases of shape reconstruction using lightness function. In both the cases, the underlying polygon is a 15-sided regular polygon with eccentricity=1. The lightness functions are measured from 30 equally spaced viewing directions in the range $[0, \pi]$ and $\sigma = 0$. For the sake of simplicity, the albedo values for all the facets of the polygon are assumed to be equal and a known value which is set equal to 1. We used the linear least squares approach given in (3.17) to obtain the estimated polygons. The only difference in the two cases is the direction w of the incoming ray of light as seen from Fig. 7.3. Clearly we can see that the quality of reconstruction is better if the viewing directions are along the brighter (more illuminated) parts of the body.

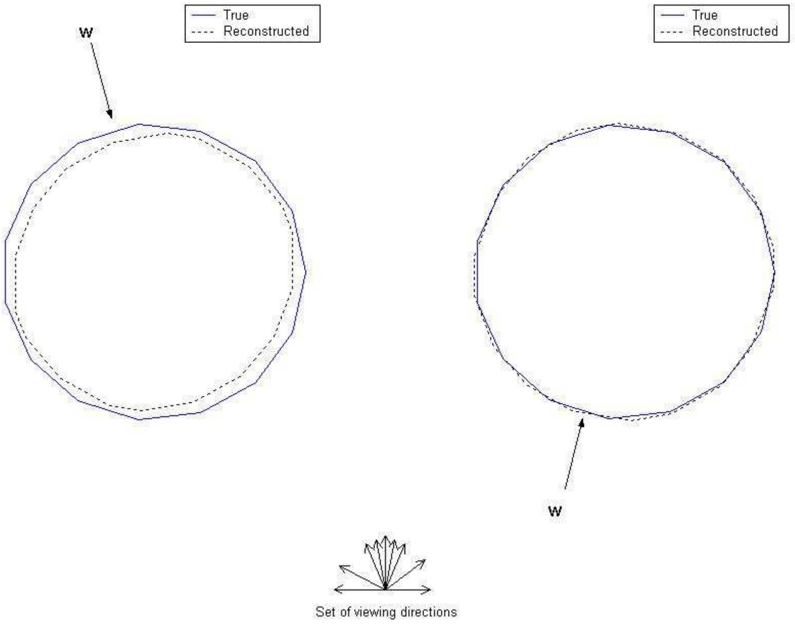

Figure 7.3: Two illustrations of shape reconstruction using Lightness Function

If the albedo value for each facet of the polygon is assumed to be unknown, the system becomes under-determined; a case which we have not yet studied. A future direction of work would also consist of developing robust algorithms for shape reconstruction using corrupted lightness function measurements. This will be of particular interest to the astronomy community; see [11]. We also need to consider the effect of having more than one light source illuminating the object. It will be also interesting to see the confidence regions for shape reconstruction using lightness functions.

7.2 Uncertainty Ellipsoids for 3-D

The algorithms for estimating the EGI using brightness functions data can be easily extended to the 3-D case; see [9] and [10]. However, the problem of estimating cartesian co-ordinates using noisy EGI values for a 3-D object is a very hard problem and has not been carefully studied in the past. The difficulty of this problem can be gauged from the fact that the obvious way to do this in the 2-D case turns out to be statistically inefficient. In the 3-D case, we are currently using the algorithm proposed by Little in [32] to obtain cartesian shape representation using pure EGI. However, we do not know yet if it is statistically efficient and whether it faces the similar problem of accumulating errors for noisy EGI. Moreover this algorithm uses non-linear optimization which makes the analysis more challenging. We can also repeat the confidence region analysis presented in this paper and generate the uncertainty ellipsoids for each vertex of the polyhedra and furthermore the uncertainty volume enclosing the underlying polyhedra.

7.3 Conclusion

In this thesis, we presented non-linear and linear algorithms for estimating a convex shape from finitely many noisy measurements of its support or brightness function. The shape was parameterized using Extended Gaussian Image and we also derived a statistically efficient method for obtaining the cartesian coordinates of a polygon from corrupted EGI values. Focusing on the 2-D case, we carried out a systematic statistical analysis of these algorithms via computation of the Cramér-Rao lower bound on the estimated parameters. Using this bound, we found local and global confidence regions for the underlying shape, providing a valuable visual demonstration of the effect of experimental parameters on the quality of estimated shape. For the support functions, the CRLB was infinity and hence we use the constrained CRLB to develop the confidence regions. Finally, we presented a performance analysis of the linear algorithm for shape from brightness functions that indicates this algorithm operates reasonably well.

Appendix A

Here we present the derivation of the Fisher Information Matrix (FIM) for support and brightness function measurements.

A.1 FIM calculation for Brightness Functions

In this section, we present the analysis for the case of brightness functions. The measurement model for brightness function measurements of a planar convex body is,

$$b(\alpha_m) = \frac{1}{2}\sum_{k=1}^{N} a_k|\cos(\alpha_m - \theta_k)| + n(\alpha_m)$$

where, $m = 1, \ldots, M$ and M = total number of observations.

N = total number of edges of the polygon.

$\alpha_m = m^{th}$ viewing direction

θ_k = Normal to the k^{th} side of the polygon

a_k = Length of the k^{th} side of the polygon

$b(\alpha_m)$ = brightness function measurement along the viewing direction α_m

$n(\alpha_m)$ = Noise corrupting the brightness function measurement along the direction α_m (assumed to be White Gaussian Noise with zero mean and variance σ^2).

If the underlying body is origin symmetric, the joint PDF of the observed data can be obtained from (5.9) as follows,

$$p_b(\mathbf{x};\mathbf{\Psi}) = \prod_{m=1}^{M} \frac{1}{\sqrt{2\pi\sigma^2}} \exp\left[-\frac{1}{2\sigma^2}\left(b(\alpha_m) - \sum_{k=1}^{N/2} a_k|\cos(\alpha_m-\theta_k)|\right)^2\right]$$

where the $\mathbf{x} = [b(\alpha_1),\ldots,b(\alpha_M)]^T$ and $\mathbf{\Psi} = [a_1,\ldots,a_{N/2},\theta_1,\ldots,\theta_{N/2}]^T$.

Therefore, the log-likelihood function for the brightness data is given as,

$$\ln p_b(\mathbf{x};\mathbf{\Psi}) = -\frac{M}{2}\ln(2\pi\sigma^2) - \frac{1}{2\sigma^2}\sum_{m=1}^{M}\left(b(\alpha_m) - \sum_{k=1}^{N/2} a_k|\cos(\alpha_m-\theta_k)|\right)^2 \tag{A.1}$$

To calculate $\mathbf{J_1}(i,j)$

$$\mathbf{J_1}(i,j) = -E\left(\frac{\partial^2 \ln p_b(\mathbf{x};\mathbf{\Psi})}{\partial a_i \partial a_j}\right) \text{ for } i,j = 1,\ldots,N/2 \tag{A.2}$$

Differentiating the log-likelihood function (A.1) wrt the parameter a_i we get,

$$\begin{aligned}\frac{\partial \ln p_b(\mathbf{x};\mathbf{\Psi})}{\partial a_i} &= -\frac{1}{2\sigma^2}\sum_{m=1}^{M}\left[2\left(b(\alpha_m) - \sum_{k=1}^{N/2} a_k|\cos(\alpha_m-\theta_k)|\right)\frac{\partial}{\partial a_i}\left(-\sum_{k=1}^{N/2} a_k|\cos(\alpha_m-\theta_k)|\right)\right]\\ &= \frac{1}{\sigma^2}\sum_{m=1}^{M}\left[\left(b(\alpha_m) - \sum_{k=1}^{N/2} a_k|\cos(\alpha_m-\theta_k)|\right)|\cos(\alpha_m-\theta_i)|\right] \end{aligned} \tag{A.3}$$

Differentiating (A.3) wrt the parameter a_j we get,

$$\frac{\partial^2 \ln p_b(\mathbf{x};\mathbf{\Psi})}{\partial a_i \partial a_j} = -\frac{1}{\sigma^2}\sum_{m=1}^{M}\left(|\cos(\alpha_m-\theta_i)||\cos(\alpha_m-\theta_j)|\right) \tag{A.4}$$

Therefore, from (A.2) and (A.4) we obtain,

$$\mathbf{J_1}(i,j) = \frac{1}{\sigma^2}\sum_{m=1}^{M}\left(|\cos(\alpha_m-\theta_i)||\cos(\alpha_m-\theta_j)|\right)$$

To calculate $\mathbf{J_2}(i,j)$ and $\mathbf{J_3}(i,j)$

$$\mathbf{J_3}(i,j) = \mathbf{J_2}(j,i) = -E\left(\frac{\partial^2 \ln p_b(\mathbf{x};\mathbf{\Psi})}{\partial \theta_i \partial a_j}\right) \text{ for } i,j = 1,\ldots,N/2$$

Differentiating the log-likelihood function (A.1) wrt the parameter θ_i we get,

$$\begin{aligned}
\frac{\partial \ln p_b(\mathbf{x};\mathbf{\Psi})}{\partial \theta_i} &= -\frac{1}{2\sigma^2}\sum_{m=1}^{M}\left[2\left(b(\alpha_m)-\sum_{k=1}^{N/2}a_k|\cos(\alpha_m-\theta_k)|\right)\frac{\partial}{\partial \theta_i}\left(-\sum_{k=1}^{N/2}a_k|\cos(\alpha_m-\theta_k)|\right)\right]\\
&= \frac{1}{\sigma^2}\sum_{m=1}^{M}\left[\left(b(\alpha_m)-\sum_{k=1}^{N/2}a_k|\cos(\alpha_m-\theta_k)|\right)\frac{\partial}{\partial \theta_i}\left(a_i|\cos(\alpha_m-\theta_i)|\right)\right]\\
&= \frac{a_i}{\sigma^2}\sum_{m=1}^{M}\left[\left(b(\alpha_m)-\sum_{k=1}^{N/2}a_k|\cos(\alpha_m-\theta_k)|\right)sign(\cos(\alpha_m-\theta_i))\sin(\alpha_m-\theta_i)\right] \quad (A.5)
\end{aligned}$$

Differentiating (A.5) wrt a_j we get,

$$\begin{aligned}
\frac{\partial^2 \ln p_b(\mathbf{x};\mathbf{\Psi})}{\partial \theta_i \partial a_j} &= \frac{a_i}{\sigma^2}\sum_{m=1}^{M}\left[sign(\cos(\alpha_m-\theta_i))\sin(\alpha_m-\theta_i)\frac{\partial}{\partial a_j}\left(-\sum_{k=1}^{N/2}a_k|\cos(\alpha_m-\theta_k)|\right)\right]\\
&= -\frac{a_i}{\sigma^2}\sum_{m=1}^{M}sign(\cos(\alpha_m-\theta_i))\sin(\alpha_m-\theta_i)|\cos(\alpha_m-\theta_j)| \quad (A.6)
\end{aligned}$$

Therefore,

$$\mathbf{J_3}(i,j)=\mathbf{J_2}(j,i)=\frac{a_i}{\sigma^2}\sum_{m=1}^{M}sign(\cos(\alpha_m-\theta_i))\sin(\alpha_m-\theta_i)|\cos(\alpha_m-\theta_j)| \quad (A.7)$$

To calculate $\mathbf{J_4}(i,j)$

$$\mathbf{J_4}(i,j)=-E\left(\frac{\partial^2 \ln p_b(\mathbf{x};\mathbf{\Psi})}{\partial \theta_i \partial \theta_j}\right) \text{ for } i,j=1,\ldots,N/2$$

Differentiating (A.5) wrt θ_j we get,

$$\begin{aligned}
\frac{\partial^2 \ln p_b(\mathbf{x};\mathbf{\Psi})}{\partial \theta_i \partial \theta_j} &= \frac{a_i}{\sigma^2}\sum_{m=1}^{M}\left[sign(\cos(\alpha_m-\theta_i))\sin(\alpha_m-\theta_i)\frac{\partial}{\partial \theta_j}\left(-\sum_{k=1}^{N/2}a_k|\cos(\alpha_m-\theta_k)|\right)\right]\\
&= -\frac{a_i a_j}{\sigma^2}\sum_{m=1}^{M}sign(\cos(\alpha_m-\theta_i))\sin(\alpha_m-\theta_i)sign(\cos(\alpha_m-\theta_j))\sin(\alpha_m-\theta_j)
\end{aligned}$$

Therefore,

$$\mathbf{J_4}(i,j)=\frac{a_i a_j}{\sigma^2}\sum_{m=1}^{M}sign(\cos(\alpha_m-\theta_i))\sin(\alpha_m-\theta_i)sign(\cos(\alpha_m-\theta_j))\sin(\alpha_m-\theta_j) \quad (A.8)$$

A.2 FIM calculation for Support Functions

In this section, we present the derivation of the Fisher Information Matrix for support function data. The measurement model for support function data of a polygon having barycenter of the vertices at the origin is,

$$y(\alpha_m) = \sum_{k=1}^{N} d_{t_m k} a_k \sin(\alpha_m - \theta_k) + n(\alpha_m),$$

where the symbols have the same meaning as in Section A.1
Therefore, the joint PDF of the measured support data is given as,

$$p_h(\mathbf{y}; \mathbf{\Psi}) = \prod_{m=1}^{M} \frac{1}{\sqrt{2\pi\sigma^2}} \exp\left[\frac{-1}{2\sigma^2}\left(y(\alpha_m) - \sum_{k=1}^{N} d_{t_m k} a_k \sin(\alpha_m - \theta_k)\right)^2\right], \tag{A.9}$$

where the $\mathbf{y} = [y(\alpha_1), \ldots, y(\alpha_m)]^T$ and $\mathbf{\Psi} = [a_1, \ldots, a_N, \theta_1, \ldots, \theta_N]^T$. From (A.9), the log-likelihood function for the support data is,

$$\text{ln} p_h(\mathbf{y}; \mathbf{\Psi}) = -\frac{M}{2}\text{ln}(2\pi\sigma^2) - \frac{1}{2\sigma^2}\sum_{m=1}^{M}\left(y(\alpha_m) - \sum_{k=1}^{N} d_{t_m k} a_k \sin(\alpha_m - \theta_k)\right)^2 \tag{A.10}$$

To calculate $\mathbf{J_1}(i, j)$

$$\mathbf{J_1}(i, j) = -E\left(\frac{\partial^2 \ln p(\mathbf{y}; \mathbf{\Psi})}{\partial a_i \partial a_j}\right) \text{for } i, j = 1, \ldots, N$$

Differentiating the log-likelihood function (A.10) wrt a_i we obtain,

$$\begin{aligned}\frac{\partial \ln p_h(\mathbf{y}; \mathbf{\Psi})}{\partial a_i} &= -\frac{1}{2\sigma^2}\sum_{m=1}^{M}\left[2\left(y(\alpha_m) - \sum_{k=1}^{N} d_{t_m k} a_k \sin(\alpha_m - \theta_k)\right)\frac{\partial}{\partial a_i}\left(-\sum_{k=1}^{N} d_{t_m k} a_k \sin(\alpha_m - \theta_k)\right)\right] \\ &= \frac{1}{\sigma^2}\sum_{m=1}^{M}\left[\left(y(\alpha_m) - \sum_{k=1}^{N} d_{t_m k} a_k \sin(\alpha_m - \theta_k)\right) d_{t_m i} \sin(\alpha_m - \theta_i)\right] \end{aligned} \tag{A.11}$$

Differentiating the above equation wrt a_j we get,

$$\frac{\partial^2 \ln p_h(\mathbf{y}; \mathbf{\Psi})}{\partial a_i \partial a_j} = -\frac{1}{\sigma^2}\sum_{m=1}^{M} d_{t_m i} d_{t_m j} \sin(\alpha_m - \theta_i)\sin(\alpha_m - \theta_j) \tag{A.12}$$

Therefore, from (A.12),

$$\mathbf{J_1}(i,j) = \frac{1}{\sigma^2}\sum_{m=1}^{M} d_{t_m i} d_{t_m j} \sin(\alpha_m - \theta_i)\sin(\alpha_m - \theta_j) \tag{A.13}$$

To calculate $\mathbf{J_2}(i,j)$ and $\mathbf{J_3}(i,j)$

$$\mathbf{J_3}(i,j) = \mathbf{J_2}(j,i) = -E\left(\frac{\partial^2 \ln p(\mathbf{y};\mathbf{\Psi})}{\partial\theta_i \partial a_j}\right) \text{ for } i,j = 1,\ldots,N$$

Differentiating the log-likelihood function (A.10) wrt θ_i we obtain,

$$\begin{aligned}
\frac{\partial \ln p_h(\mathbf{y};\mathbf{\Psi})}{\partial\theta_i} &= -\frac{1}{2\sigma^2}\sum_{m=1}^{M}\left[2\left(y(\alpha_m) - \sum_{k=1}^{N} d_{t_m k} a_k \sin(\alpha_m - \theta_k)\right)\frac{\partial}{\partial\theta_i}\left(-\sum_{k=1}^{N} d_{t_m k} a_k \sin(\alpha_m - \theta_k)\right)\right] \\
&= -\frac{a_i}{\sigma^2}\sum_{m=1}^{M}\left[\left(y(\alpha_m) - \sum_{k=1}^{N} d_{t_m k} a_k \sin(\alpha_m - \theta_k)\right) d_{t_m i}\cos(\alpha_m - \theta_i)\right] \qquad \text{(A.14)}
\end{aligned}$$

Differentiating the above equation wrt a_j we get,

$$\frac{\partial^2 \ln p_h(\mathbf{y};\mathbf{\Psi})}{\partial\theta_i \partial a_j} = \frac{a_i}{\sigma^2}\sum_{m=1}^{M} d_{t_m i} d_{t_m j}\sin(\alpha_m - \theta_j)\cos(\alpha_m - \theta_i) \tag{A.15}$$

Therefore,

$$\mathbf{J_3}(i,j) = \mathbf{J_2}(j,i) = -\frac{a_i}{\sigma^2}\sum_{m=1}^{M} d_{t_m i} d_{t_m j}\sin(\alpha_m - \theta_j)\cos(\alpha_m - \theta_i) \tag{A.16}$$

To calculate $\mathbf{J_4}(i,j)$

$$\mathbf{J_4}(i,j) = -E\left(\frac{\partial^2 \ln p(\mathbf{y};\mathbf{\Psi})}{\partial\theta_i \partial\theta_j}\right) \text{ for } i,j = 1,\ldots,N$$

Differentiating (A.14) wrt θ_j we get,

$$\frac{\partial^2 \ln p_h(\mathbf{y};\mathbf{\Psi})}{\partial\theta_i \partial\theta_j} = -\frac{a_i a_j}{\sigma^2}\sum_{m=1}^{M} d_{t_m i} d_{t_m j}\cos(\alpha_m - \theta_i)\cos(\alpha_m - \theta_j) \tag{A.17}$$

Therefore,

$$\mathbf{J_4}(i,j) = \frac{a_i a_j}{\sigma^2}\sum_{m=1}^{M} d_{t_m i} d_{t_m j}\cos(\alpha_m - \theta_i)\cos(\alpha_m - \theta_j) \tag{A.18}$$

Bibliography

[1] N. Ahuja and J. Veenstra, *Generating octrees from object silhouettes in orthographic views*, IEEE Transactions on Pattern Analysis and Machine Intelligence **11** (1989), no. 2, 137–149.

[2] Andrea Bottino, Luc Jaulin, and Aldo Laurentini, *Finding feasible parameter sets for shape from silhouettes with unknown position of the viewpoints*, IEEE Transactions on Pattern Analsyis and Machine Intelligence (2003).

[3] S. Campi, A. Colesanti, and P. Gronchi, *Convex bodies with extremal volumes having prescribed brightness in finitely many directions*, Geom. Dedicata **57** (1995), 121–133.

[4] P. J. Davis, *Circulant matrices*, Willey Interscience, 1979.

[5] R. O. Duda and P. E. Hart, *Pattern classification and scene analysis*, Wiley-Interscience, 1973.

[6] N. I. Fisher, P. Hall, B. Turlach, and G. S. Watson, *On the estimation of a convex set from noisy data on its support function*, Journal of American Statistical Association **92** (1997), no. 437, 84–91.

[7] R. J. Gardner, *Geometric tomography*, Cambridge University Press, 1995.

[8] R. J. Gardner, M. Kiderlen, and P. Milanfar, *Convergence of algorithms for reconstruction from noisy support and brightness functions*, Tech. report, (in preparation), 2003.

[9] R. J. Gardner and P. Milanfar, *Shape reconstruction from brightness functions*, Proceedings of the SPIE Conference on Advanced Signal Proccessing Algorithms, Architecture, and Implementations X (2001), 234–245.

[10] R. J. Gardner and P. Milanfar, *Reconstruction of convex bodies from brightness functions*, Discrete and Computational Geometry **29** (2003), 279–303.

[11] L. Giacomini, *Asteroids shapes and rotation: what is a lightcurve?*, `http://spaceguard.ias.rm.cnr.it /tumblingstone/issues/special-palermo/ lightcurve.htm`.

[12] G. H. Golub and V. Pereyra, *The differentiation of pseudo-inverses and nonlinear least squares problems whose variables separate*, SIAM Journal of Numerical Analysis **10** (1973), 413–432.

[13] J. D. Gorman and A. O. Hero, *Lower bounds for parametric estimation with constraints*, IEEE Transactions on Imformation Theory **26** (1990), no. 6, 1285–1301.

[14] J. Gregor and F. R. Rannou, *Three-dimensional support function estimation and application for projection magnetic resonance imaging*, International Journal of Imaging System Technology **12** (2002), 43–50.

[15] H. Groemer, *On the symmetric difference metric for convex bodies*, Contributions to Algebra and Geometry **41** (2000), no. 1, 107–114.

[16] P. Hall and B. Turlach, *On the estimation of a convex set with corners*, IEEE Transactions on Pattern Analysis and Machine Intelligence **21** (1999), no. 3, 225–234.

[17] G. T. Hermann, *Image reconstruction from projections*, Academic Press, New York, 1980.

[18] B. K. P. Horn, *Robot Vision*, The MIT Press and McGraw-Hill Book Company, 1986.

[19] V. Hosel and S. Walcher, *Clustering techniques: A brief survey*, Tech. report, Institute of Biomathematics and Biometry, 2001.

[20] M. Ikehata and T. Ohe, *A numerical method for finding the convex hull of polygonal cavities using the enclosure method*, Inverse Problems **18** (2002), 111–124.

[21] A. Kak and M. Slaney, *Principles of computerized tomographic imaging*, SIAM, IEEE Press, 2001.

[22] W. C. Karl, S. R. Kulkarni, G. V. Verghese, and A. S. Willsky, *Local tests for consistency of support hyperplane data*, Journal of Mathematical Imaging and Vision **6** (1995), 249–269.

[23] S. Kay, *Fundamentals of statistical signal processing - volume II*, Prentice-Hall, Englewood Cliffs, 1993.

[24] M. Kiderlen, *Non-parameteric estimation of the directional distribution of stationary line and fibre processes*, Adv. Appl. prob. **33** (2001), 6–24.

[25] L. Lamberg, *On the minkowski problem and the lightcurve operator*, Ann. Acad. Sci. Fennicae, Math. Diss. **87** (1993).

[26] A. Laurentini, *The visual hull concept for silhouette-based image understanding*, IEEE Transactions on Pattern Analysis and Machine Intelligence **16** (1994), no. 2, 150–162.

[27] A. S. Lele, S. R. Kulkarni, and A. S. Willsky, *Convex polygon estimation from support line measurements and applications to target reconstruction from laser radar data*, Journal of Optical Society America **9** (1992), 1693–1714.

[28] J. Lemordant, P. D. Tao, and H. Zouaki, *Modélisation et optimisation numérique pour la reconstruction d'un polyèdre à partir de son image gaussienne généralisée,*, RAIRO Modél. Math. Anal. Numér. **27** (1993), 349–374.

[29] S. Y. R. Li, *Reconstruction of polygons from projections*, Information Processing Letters **28**, 235–240.

[30] M. Lindenbaum and A. Bruckstein, *Reconstructing a convex polygon from binary perspective projections*, Pattern Recognition **23** (1990), no. 12, 1343–1350.

[31] M. Lindenbaum and A. Bruckstein, *Blind approximation of planar convex sets*, IEEE Transaction on Robotics and Automation **10** (1994), no. 4, 517–529.

[32] J. J. Little, *An iterative method for reconstructing convex polyhedra from extended gaussian images*, Proceedings AAAI National Conference on Artificial Intelligence (1983), 247–250.

[33] E. Mammen, J. S. Marron, B. A. Turlach, and M. P. Wand, *A general projection framework for constrained smoothing*, Statistical Sciences **16** (2001), no. 3, 232–248.

[34] K. V. Mardia and P. E. Jupp, *Directional statistics*, Willey, 2001.

[35] W. N. Martin and J. K. Agarwal, *Volumetric description of objects from multiple views*, IEEE Transactions on Pattern Analysis and Machine Intelligence **5** (1983), 150–158.

[36] J. L. Prince, *Geometric model-based estimation from projections*, Ph.D. thesis, Massachusetts Institute of Technology, 1988.

[37] J. L. Prince and A. S. Willsky, *Estimating convex sets from noisy support line*

measurements, IEEE Transactions on Pattern Analysis and Machine Intelligence **12** (1990), no. 4, 377–389.

[38] A. S. Rao and K. Y. Goldberg, *Shape from diameter: Recognizing polygonal parts with a parallel-jaw gripper*, International Journal of Robotics Research **13** (1994), no. 1, 16–37.

[39] R. Schneider, *Convex bodies: The brunn-minkowski theory*, Cambridge University Press, 1993.

[40] P. Stoica and B. C. Ng, *On the cramér-rao bound under parametric constraints*, IEEE Signal Processing Letters **5** (1998), no. 7, 177–179.

[41] M. A. Sumbatyan and E. A. Troyan, *Reconstruction of the shape of a convex defect from a scattered wave field in the ray approximation*, Journal of Applied Mathematics and Mechanics **56** (1992), 464–468.

[42] E. C. Veltkamp, *Shape matching: similarity measures and algorithms*, Proceedings of the International Conference on Shape Modelling and Applications (2001), 188–197.

[43] J. C. Ye, Y. Bresler, and P. Moulin, *Asymptotic global confidence regions in parametric shape estimation problems*, IEEE Transactions on Information Theory **46** (2000), no. 5, 1881–1895.

[44] Pan Zhingeng, Zhou Kun, and Shi Jiaoying, *A new mesh simplification algorithm based on triangle collapses*, Journal of Computer Science and Technology **16** (2001), no. 1, 57–63.